Geosci. Model Dev., 15, 3253–3279, 2022
https://doi.org/10.5194/gmd-15-3253-2022

Geoscientific Model Development
Open Access
EGU

Estimating aerosol emission from SPEXone on the NASA PACE mission using an ensemble Kalman smoother: observing system simulation experiments (OSSEs)

Athanasios Tsikerdekis[1,2], Nick A. J. Schutgens[2], Guangliang Fu[1], and Otto P. Hasekamp[1]

[1]Earth Group, SRON Netherlands Institute for Space Research, 2333 CA Leiden, the Netherlands
[2]Department of Earth Science, Vrije Universiteit Amsterdam, 1081 HV Amsterdam, the Netherlands

Correspondence: Athanasios Tsikerdekis (a.tsikerdekis@sron.nl)

Received: 19 August 2021 – Discussion started: 2 November 2021
Revised: 7 February 2022 – Accepted: 10 March 2022 – Published: 21 April 2022

Abstract. We present a top-down approach for aerosol emission estimation from Spectropolarimeter for Planetary Exploration (SPEXone) polarimetric retrievals related to the aerosol amount, size, and absorption using a fixed-lag ensemble Kalman smoother (LETKS) in combination with the ECHAM-HAM model. We assess the system by performing observing system simulation experiments (OSSEs) in order to evaluate the ability of the future multi-angle polarimeter instrument, SPEXone, as well as a satellite with near-perfect global coverage. In our OSSEs, the nature run (NAT) is a simulation by the global climate aerosol model ECHAM-HAM with altered aerosol emissions. The control (CTL) and the data assimilation (DAS) experiments are composed of an ensemble of ECHAM-HAM simulations, where the default aerosol emissions are perturbed with factors taken from a Gaussian distribution. Synthetic observations, specifically aerosol optical depth at 550 nm (AOD_{550}), Ångström exponent from 550 to 865 nm ($AE_{550–865}$), and single-scattering albedo at 550 nm (SSA_{550}) are assimilated in order to estimate the aerosol emission fluxes of desert dust (DU), sea salt (SS), organic carbon (OC), black carbon (BC), and sulfate (SO_4), along with the emission fluxes of two SO_4 precursor gases (SO_2, DMS). The prior emission global relative mean absolute error (MAE) before the assimilation ranges from 33 % to 117 %. Depending on the species, the assimilated observations sampled using the satellite with near-perfect global coverage reduce this error to equal to or lower than 5 %. Despite its limited coverage, the SPEXone sampling shows similar results, with somewhat larger errors for DU and SS (both having a MAE equal to 11 %). Further, experiments show that doubling the measurement error increases the global relative MAE up to 22 % for DU and SS. In addition, our results reveal that when the wind of DAS uses a different reanalysis dataset (ERA5 instead of ERA-Interim) to the NAT, the estimated SS emissions are negatively affected the most, while other aerosol species are negatively affected to a smaller extent. If the DAS uses dust or sea salt emission parametrizations that are very different from the NAT, posterior emissions can still be successfully estimated, but this experiment revealed that the source location is important for the estimation of dust emissions. This work suggests that the upcoming SPEXone sensor will provide observations related to aerosol amount, size, and absorption with sufficient coverage and accuracy in order to estimate aerosol emissions.

1 Introduction

Data assimilation methods can greatly improve the aerosol representation in the atmosphere by combining the simulated aerosol state of a model with the observed aerosol optical and microphysical properties retrieved from satellites. The accuracy of the spatiotemporal distribution of an aerosol species in a data assimilation product depends both on the accuracy of the simulated processes in the model as well as the quality and the type of the assimilated observations. Several past studies estimated aerosol emission based on remote sensing observations (Dubovik et al., 2008; Jin et al., 2019; Pope et al., 2016; Sekiyama et al., 2010; Xu et al., 2013), although only some studies assimilated size related

measurements, such as aerosol optical depth (AOD) in two wavelengths or fine and coarse AOD or Ångström exponent (AE) (Escribano et al., 2017; Huneeus et al., 2012; Schutgens et al., 2012). In addition, very few recent studies assimilated absorption-related measurements like absorption aerosol optical depth (AAOD) or single-scattering albedo (SSA) to correct either the aerosol mixing ratio (Tsikerdekis et al., 2021a) or the aerosol emissions (Chen et al., 2018, 2019). Absorption observations were used by Kacenelenbogen et al. (2019) to estimate the short-wave direct aerosol effect from the A-Train satellite sensors. Further, Schutgens et al. (2021) intercompared and evaluated four AERONET satellite products (FL-MOC, OMAERUV, POLDER-GRASP, and POLDER-SRON) for AAOD and SSA and suggested that satellite absorption observations could be used to evaluate AEROCOM model biases because the diversity of model biases is larger than satellite biases.

It has been noted in the past that multi-viewing angle and multi-wavelength intensity and polarization measurements with high accuracy have the largest capability to provide the aerosol properties relevant to climate research (Hasekamp and Landgraf, 2007). Recently, Hasekamp et al. (2019b) showed that polarimetric satellite retrievals related to aerosol shape, size, and number provide a more accurate aerosol indirect radiative effect compared to previous observational-based studies. Unfortunately only one such multi-angle polarimeter (MAP) provided aerosol optical and microphysical properties from space for several years in the past (2004–2013), the Polarization and Directionality of Earth Reflectances (POLDER-3) on board the microsatellite PARASOL (Dubovik et al., 2019).

Several MAP instruments are scheduled for launch in the coming 3 years (Dubovik et al., 2019), with the NASA PACE mission (Werdell et al., 2019) hosting two MAP sensors onboard, the Spectropolarimeter for Planetary Exploration SPEXone (Hasekamp et al., 2019a) and the Hyper-Angular Rainbow Polarimeter-2 (HARP-2). Since these instruments are not yet in space, their observational capabilities for aerosol optical properties (and consequently their potential to estimate aerosol-species-specific emission fluxes) can only be theoretically predicted with observing system simulation experiments (OSSEs) (Arnold and Dey, 1986; Timmermans et al., 2015). In OSSEs a model simulation is assumed as reality, also known as the nature run (NAT), from which synthetic measurements are sampled based on the spatiotemporal coverage of an assumed satellite sensor. Subsequently, two experiments are conducted, a control (CTL) and a data assimilation (DAS) experiment, in which the sampled synthetic observations from the NAT are assimilated. Note that the NAT and the CTL simulations are different experiments, either by using a totally different model or by using the same model with different emissions and/or physics options. The ability of the instrument to estimate the aerosol state can be highlighted by evaluating the CTL and the DAS experiments with NAT.

Timmermans et al. (2008) firstly used OSSEs with an ensemble Kalman filter to assess the ability of assimilated AOD sampled based on an imager type instrument and assimilated $PM_{2.5}$ sampled based on the location of ground based stations, with the goal to estimate $PM_{2.5}$ concentrations over Europe. Meland et al. (2013) used OSSEs with an adjoint inverse data assimilation method for aerosol emission estimation to assess the benefits of remote polarimetric measurements over intensity measurements. Even though the intensity measurements had broader spatial coverage, aerosol emissions were 3 times more sensitive to the polarized reflectance at the top of the atmosphere compared to the radiant reflectance at the top of the atmosphere. In addition, it was highlighted that assimilated multi-angle polarimetric measurements could substantially improve aerosol simulations. Subsequent studies using real POLDER retrievals confirmed this for aerosol mixing ratio estimation (Tsikerdekis et al., 2021a) and aerosol emission estimation (Chen et al., 2019) from the POLDER-3 instrument. Yumimoto and Takemura (2013) used OSSEs and a 4D-Var data assimilation system to estimate aerosol emissions based on simulated observations of fine- and coarse-mode AOD sampled based on the Moderate Resolution Imaging Spectrometer (MODIS). Khade et al. (2013) explored the possibility to estimate soil erodibility factors (that drive dust emissions) by assimilating satellite AOD in an ensemble adjustment Kalman filter. Xu et al. (2017) showed the usefulness of assimilating both reflected solar and infrared radiances from the CLARREO's mission to accurately constrain size-resolved aerosol emissions for four dust size bins. Further, they concluded that CLARREO data failed to constrain dust sources due to its narrow swath, and the combination of narrow and wide swath observations might be more desirable. The full scope of PACE mission observations, which include a narrow (SPEXone) and a wide (HARP-2) swath polarimeter, as well as a wide swath radiometer (OCI), would possibly be able to bring this idea into practice.

In this study we quantify how well an instrument with high accuracy but limited coverage, like SPEXone, can estimate aerosol emissions. Under the framework of OSSEs, we implement an existing local ensemble transform Kalman smoother (LETKS) code to operate with the global aerosol climate model ECHAM-HAM and assimilate synthetic observations based on a future multi-angle polarimeter instrument (SPEXone) and a theoretical satellite with near-perfect global coverage. Following the results of our previous work and based on the MAP observational capabilities of SPEXone, we assimilate AOD_{550}, $AE_{550–865}$, and SSA_{550} in order to encompass information related to aerosol mass, size, and absorption (Tsikerdekis et al., 2021a). In Sect. 2, the SPEXone instrument on PACE and the aerosol climate model ECHAM-HAM are described, along with the spatiotemporal coverage and uncertainties of SPEXone and of an idealized instrument. Section 3 presents the data assimilation system, its newly developed features, and the experimental setup. Fi-

nally, in Sect. 4 the ability of SPEXone to estimate emissions is presented, along with SPEXone sensitivity experiments and other sensitivity experiments that explore uncertainty factors that can affect the emission estimation.

2 Data

2.1 SPEXone on PACE

SPEXone is a passive remote sensing MAP instrument, part of the NASA Plankton, Aerosol, Cloud, and ocean Ecosystem (PACE) mission (Werdell et al., 2019), scheduled for launch in 2023/2024. It was developed by the Netherlands Institute for Space Research (SRON) and the Airbus Defense and Space Netherlands (ADS-NL) with optical expertise from the Netherlands Organization for Applied Scientific Research (TNO). SPEXone can measure intensity and polarization of backscattered sunlight at multiple wavelengths and discrete viewing angles for a specific pixel on the ground. Specifically, it can measure radiance and polarization at five viewing angles ($+57$, $+20$, 0, -20, -57° on ground) with high accuracy (0.003) in the degree of linear polarization (DoLP). SPEXone is a spectrometer, measuring a continuous spectrum (at 2 nm resolution for radiance and 10–25 nm for polarization) between the spectral range from 385 to 770 nm. The sensor's horizontal resolution is $\sim 5.4 \times 4.6$ km for all viewing angles, and the swath is 100 km. The aerosol-retrieved parameters include column AOD, AE, SSA, aerosol layer height, effective radius, effective variance (of the size distribution), complex refractive index, particle number for a fine- and a coarse-mode aerosol, and a shape parameter for the coarse mode. Detailed information on the optical and technical attributes and the retrieval capabilities of SPEXone can be found in Hasekamp et al. (2019a) and van Amerongen et al. (2019).

2.2 The ECHAM6-HAM2 aerosol climate model

The sixth generation of the general circulation model ECHAM6, developed at the Max Planck Institute for Meteorology (MPI-M) in Hamburg, Germany (Stevens et al., 2013), and the second version of the Hamburg Aerosol Model (HAM2) (Stier et al., 2005; Tegen et al., 2019; Zhang et al., 2012) are used to simulate the physical and chemical processes of aerosol in the atmosphere.

The M7 aerosol module used in HAM2 considers five aerosol species, dust (DU), sea salt (SS), organic carbon (OC), black carbon (BC), and sulfates (SO_4) (Vignati et al., 2004). Aerosols are partitioned into seven unimodal lognormal particle size distributions (nucleation, Aitken, accumulation, coarse) called modes and separated into two hygroscopic classes (hydrophobic and hydrophilic). Six of these modes contain several aerosol species (internally mixed modes). Each mode is characterized by the number concentration and the mass concentration by species. Aerosol number and mass are used in order to calculate the median radius for each mode (Tegen et al., 2019). The mode width (standard deviation of the lognormal distribution) is assumed and fixed as equal to 1.59 for the nucleation, Aitken, and accumulation modes and 2.00 for the coarse mode. The cloud and aerosol optical properties are computed using Mie theory and derived from lookup tables (Tegen et al., 2019) using the prognostic concentrations of aerosol tracers (Schultz et al., 2018).

All aerosol species are emitted, transported, deposited, and take part in aerosol–radiation interactions (scattering and absorption) and aerosol microphysical processes (e.g., nucleation, coagulation, aerosol water uptake, and cloud activation). The natural aerosol types (DU, SS) are introduced to the atmosphere by utilizing the simulated information of wind and certain surface and ocean characteristics. Other aerosol species (OC, BC) or aerosol precursor gases (SO_2, DMS) that are emitted from both natural (e.g., forest fires) and anthropogenic sources use predefined emission inventories (Zhang et al., 2012). For a description of the importance of individual processes, see the budget sorted by species in Schutgens and Stier (2014).

Two SS emission schemes are used in this study. The first and default scheme in ECHAM-HAM parameterizes sea salt emissions based on laboratory measurements (Keene et al., 2007) using the wind velocity at 10 m and the sea surface temperature (SST) (Long et al., 2011; Sofiev et al., 2011). Low SST results in lower sea salt emissions with smaller particle size (Sofiev et al., 2011). The second scheme (previously the default option) in ECHAM-HAM calculates the sea salt flux mass and number through tables of wind speed classes and fits to two lognormal distributions based on Guelle et al. (2001 and reference therein). Note that sea salt particles are emitted only in the soluble accumulation and coarse mode in both schemes.

Dust emissions are based on the dust source scheme developed by Tegen et al. (2002). Wind velocity at 10 m is the main driver of dust aerosol particle production, while soil properties are also taken into account. The preferential dust emission sources are consist of arid or sparsely vegetated areas and are predefined based on Tegen et al. (2002). Improvements in the surface aerodynamic roughness length, soil moisture, and soil properties over East Asia specifically were made by Cheng et al. (2008). The threshold friction velocity depends on the soil size distribution, vegetation cover, and soil moisture (Cheng et al., 2008). Further, updates related to the representation of Saharan dust sources were made using infrared dust index from the SEVIRI instrument on board the Meteosat second-generation satellite by Heinold et al. (2016).

The emission for the remaining aerosol types and aerosol precursors are defined using emission inventories derived for 14 sectors. Each sector may include one or more aerosol types or aerosol precursors (Schultz et al., 2018; Tegen et al., 2019). The Atmospheric Chemistry and Climate Model Intercomparison Project (ACCMIP) dataset is used for the

anthropogenic, biomass burning, and aerosol precursor emissions, consisting of monthly mean estimates at a horizontal resolution $0.5° \times 0.5°$ (Lamarque et al., 2010). The Community Emissions Data System (CEDS) is used as an alternative for the anthropogenic aerosol and aerosol precursor (Hoesly et al., 2018). The first version of Global Fire Assimilation System (GFAS) is also used for the biomass burning emissions coming from grass and forest fires consisting of daily gridded estimates at $0.5° \times 0.5°$ horizontal resolution based on the fire radiative power measurements of the MODIS instrument (Kaiser et al., 2012). A more detailed description of both ECHAM6 and HAM2 can be found in Tegen et al. (2019).

3 Methods

3.1 Local ensemble transform Kalman smoother

The local ensemble transform Kalman smoother (LETKS) is used to estimate aerosol emission fluxes. This method has been previously used by Schutgens et al. (2012) for aerosols emission estimation and earlier by Bruhwiler et al. (2005), Peters et al. (2005), and Feng et al. (2009) for CO_2 emission estimation. It requires a model to produce background information based on assumed emissions and observations that are assimilated to estimate analysis emissions. In data assimilation studies the terms analysis or posterior are used to describe the improved state of the system due to assimilation, although in this study we reserve the term analysis for cases where the aerosol emissions were estimated by a fraction of the total observations that are going to affect them in the end (more details follow).

The data assimilation occurs in assimilation cycles, where each cycle contains a background and an analysis step as depicted in Fig. 1. Dashed boxes indicate the default emission where no assimilation took place yet, while filled boxes indicate emission changed based on observations. The background step consists of an 8 d (ΔT_b) forward simulation of the model that will initially (first cycle) create the simulated background observations. Following this, all the available observations within the last 2 d (ΔT_s) of the forward simulation are assimilated in order to estimate the analysis emission for the last 6 d ($\Delta T_a = \Delta T_b - \Delta T_s$) of the forward simulation. Note here that the term analysis is used to indicate the updated emissions affected by n days of observations (where $n < \Delta T_a$), while the term posterior is used to indicate updated emissions affected by ΔT_a days of observations (Fig. 1). This is where the first cycle ends. In the second cycle, background emissions are set as equal to the analysis emissions of the first cycle, and the respective steps of the background and assimilation steps are then performed for the second cycle. This process continues until the end of the assimilation experiment.

The assimilation window (ΔT_s) defines the shift (step) in time of the forward simulation in each cycle, the period of the assimilated observations, and the period during which emissions are estimated. A $\Delta T_s = 2$ d allows the aggregation of more satellite observations that provides a better constraint on emission estimates globally, but it also assumes that emissions do not change considerably over this period. Undoubtedly this is not always the case, for example dust emissions may vary a lot from day to day. The smoother lag (ΔT_a) determines how many days are going to be affected by the assimilated observations in one assimilation cycle. In our setup this is equal to 6 d, but we conduct experiments to see its impact when reduced to 4 and 2 d.

Note that it is assumed that the observations of a certain day contain only a fraction of the available information to change the emissions and that the rest is contained in observations of subsequent days. Thus, emissions should be estimated iteratively, allowing observations up to 6 d after to correct the emissions. The posterior emission perturbations, corrected by 6 d of observations, are derived after three assimilation cycles and are indicated with an asterisk (*) in Fig. 1. For example, the posterior emission perturbations for days 7 and 8 are estimated in the third assimilation cycle and are corrected from the assimilated observations of days 7 to 12.

Background emissions come with uncertainties. The uncertainty of background emissions are represented by an ensemble that is generated by perturbing the default emissions. The perturbations are not globally constant but vary from grid cell to grid cell. Each grid cell has a distinct prior emission distribution. Changes in neighboring grid cells of each member are not abrupt but smooth. This spatial correlation of the prior perturbations was generated using spatial smoothing, a method where data points are averaged with their neighbors. A step-by-step description of how our spatially correlated perturbations are created can be found at Sect. 3.2 of our preceding work (Tsikerdekis et al., 2021a). The spatial correlation length scale of the generated perturbations is approximately 25° omnidirectionally. The perturbations are uniquely created and distinctively estimated by the data assimilation system for each aerosol species and sulfate precursor gas. The resulting 2D spatially correlated perturbations are multiplied with the model's emissions for each aerosol species and each member, resulting in an ensemble of simulations. In our experiments the ensemble size is 32. Note that the mean and the standard deviation of background distribution is equal to 1. Furthermore, it is noted that the perturbations are uniquely defined every $\Delta T_s = 2$ d (different colors in the boxes of Fig. 1). The rationale here is that the simulated observations and emissions at day D (where D is any integer number) will be more correlated than the simulated observations at day $D + \Delta T_s$ and emissions at day D. Consequently, changes in emissions caused by assimilated observations of day D will be stronger compared to changes in emissions by assimilated observations of day $D + \Delta T_s$. This

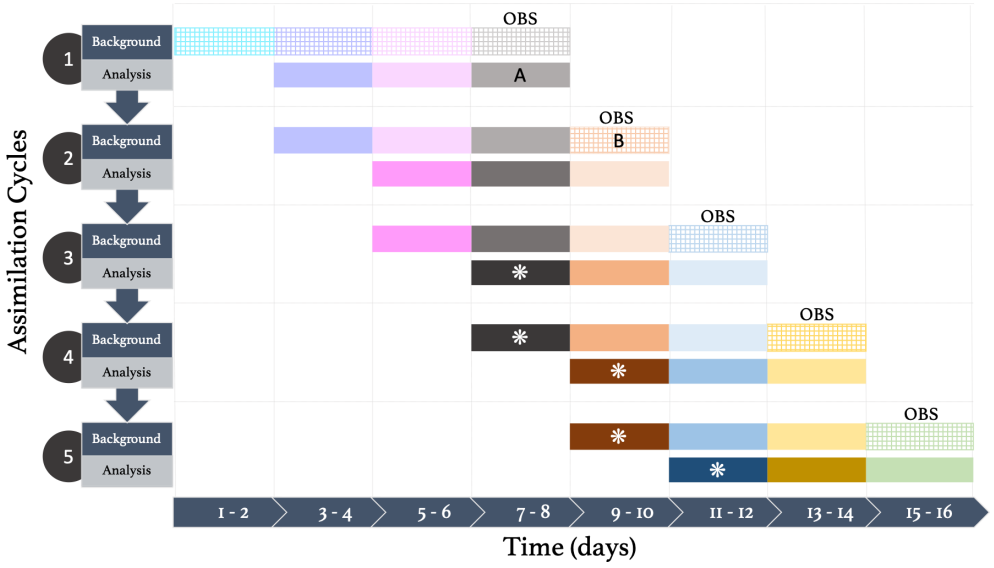

Figure 1. An illustration of the data assimilation system. The horizontal axis depicts time in segment of 2 d and the vertical axis the assimilation cycles, where each consist of a background and an analysis step. Boxes consist of 32 spatially correlated perturbation maps for each perturbed parameter (DU, SS, OC, BC, SO_4, SO_2, and DMS) that are used to create the ensemble. Dashed colored boxes indicate the default perturbations where the ensemble mean and standard deviation are equal to 1. Solid colored boxes express the analysis emission perturbations that were affected by the assimilation of some observations. Solid colored boxes with an asterisk (*) show the posterior emission perturbations corrected based on 6 d of observations. Different colors signify that different perturbations are used every 2 d. "OBS" indicates the assimilated observations for a 2 d period. A and B are marked in order to explain the prior correction (Sect. 3.2).

design is based on the fact that observations on the day of the emissions carry more information about the emissions than observations in subsequent days.

More info regarding the emission perturbations and the ensemble can be found in our preceding work (Tsikerdekis et al., 2021a). New emission estimates are obtained by estimating new perturbed emission factors based on the assimilated observations by solving the Kalman filter equations:

$$\boldsymbol{x}_\mathrm{a} = \boldsymbol{x}_\mathrm{b} + \mathbf{P}_\mathrm{a} \cdot \mathbf{H}^\mathrm{T} \cdot \mathbf{R}^{-1} \cdot (\boldsymbol{y} - \mathbf{H} \cdot \boldsymbol{x}_\mathrm{b}), \quad (1)$$

$$\mathbf{P}_\mathrm{a} = (I + \mathbf{P}_\mathrm{b} \cdot \mathbf{H}^\mathrm{T} \cdot \mathbf{R}^{-1} \cdot \mathbf{H})^{-1} \cdot \mathbf{P}_\mathrm{b}, \quad (2)$$

where $\boldsymbol{x}_\mathrm{b}$ is the background state vector and represents the variables aimed to be improved. It includes emission perturbations of five aerosol species (DU, SS, OC, BC, SO_4) and the emission perturbations of two aerosol precursor gases (SO_2, DMS). $\boldsymbol{x}_\mathrm{a}$ is the analysis state vector, which is the improved version of $\boldsymbol{x}_\mathrm{b}$ based on the assimilated observations ($\boldsymbol{y}$). The background and analysis uncertainty and correlations of emission are represented by the model error covariance matrix $\mathbf{P}_\mathrm{b}$ and $\mathbf{P}_\mathrm{a}$ respectively, using the ensemble. The observational uncertainties are represented by the error covariance matrix $\mathbf{R}$. We assume $\mathbf{R}$ to be diagonal (i.e., correlations between observational errors are assumed to always be zero). The observational operator $\mathbf{H}$ translates the emission perturbations ($\boldsymbol{x}$) to the simulated observations ($\mathbf{H} \cdot \boldsymbol{x}$) and is entirely handled by the model (emission, transport, deposition, aerosol processes, and optical properties code). T stands for the matrix transpose operator.

3.2 LETKS smoother prior correction

The ensemble Kalman filter assumes that prior emissions in the model are unbiased. In reality this is not necessarily the case, since emission inventories or emission schemes in models may suffer from biases that are often higher than the defined background uncertainty. Past studies have demonstrated that optimizing prior emissions based on previous assimilation cycles can improve data assimilation performance (Bruhwiler et al., 2005; Peng et al., 2017; Peters et al., 2005). Based on that we have developed a method, hereafter called the "prior correction". Prior correction updates the prior emission based on estimated emissions from the previous assimilation cycles, thus correcting biased emissions of the model as the data assimilation experiment progresses in time. Specifically, the ensemble mean (E_mean) of the new emission perturbations of each cycle is defined according to the analysis results of the previous assimilation cycle. For example, the E_mean of the newly created perturbations at B (Fig. 1) will be equal to the E_mean of the perturbation at A (Fig. 1). Consequently, the filter corrects the emissions bias based on the estimated emissions of previous assimilation cycles.

Although prior correction fixes the problem of potentially biased model prior emissions, it may introduce unwanted

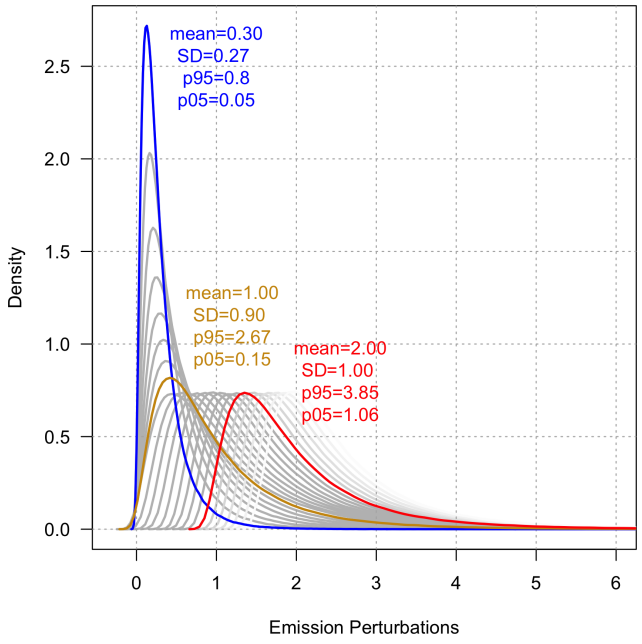

Figure 2. An example that shows how the ensemble standard deviation (E_{std}) is scaled according to the ensemble mean (E_{mean}) with the prior correction option. Although each distribution appears smooth for illustrative purposes, they consist of 32 emission perturbation values, equal to our ensemble size. Blue, yellow, and red curves highlight the statistics of three distributions with an ensemble mean of 0.3, 1, and 2, respectively. The 95 % (p95) and 5 % (p05) percentile indicate the approximate highest and lowest value of an ensemble member in these distributions. Grey curves represent in-between distribution shapes (other than the ones highlighted) with different ensemble means.

negative emission perturbations when the E_{mean} drops below 1. One way of addressing this issue would be to set all negative produced perturbations to zero, but this will affect the distribution of the perturbations and make it less Gaussian. Hence, the ensemble standard deviation (E_{std}) is adjusted according to the E_{mean}:

$$E_{\text{mean}} \leq 1.1 \rightarrow E_{\text{std}} = 1, \quad (3)$$

$$E_{\text{mean}} > 1.1 \rightarrow E_{\text{std}} = E_{\text{mean}} \cdot 0.9. \quad (4)$$

As an example, three distributions with different E_{mean} and adjusted E_{std} are depicted in Fig. 2. Note that even under this design there is <0.5 % chance to generate a negative value in the distribution when E_{mean} is lower than 1, which in that case is set to zero. The adjusted E_{std} method implies that emissions will have lower relative background uncertainty when E_{std}<1.1. This might not benefit the data assimilation system for some dust sources where emissions can differ substantially from day to day, although we have not noticed examples where this is a problem.

The prior correction approach has two optional settings where the background E_{mean} can reach a maximum or a minimum threshold. Under the framework of OSSEs, these background minimum and maximum values are known, since the background and the nature emissions can be compared. However, in reality these values can only be approximated using observations; for example, this can be done by using the ratio of background simulated observations to real observations. The majority of the experiments with the prior correction option use a minimum and a maximum threshold equal to 0.3 and 3.6, respectively, based on the AOD ratio of NAT to CTL. It is noted, however, that AOD is just one of the assimilated observations that constrains the emissions and that further work is needed in case background minimum and maximum settings are used in a data assimilation experiment with real observations. The effect of prior correction is tested by conducting two data assimilation experiments (with and without prior correction) that are presented in Appendix A.

3.3 Observing system simulation experiments (OSSEs)

Observing system simulation experiments (OSSEs) are data assimilation experiments in which synthetic observations are used that themselves are generated by a model. The synthetic observations of an OSSE can be modified to match the spatiotemporal coverage and observational uncertainty of any satellite sensor. Hence, with OSSEs it is possible to assess the potential impact of past, present, and future satellite missions on aerosol top-down emission estimation. The unique advantage of OSSEs is that the "truth" is perfectly known for all times, locations, and climate and aerosol components and can be used to evaluate the performance of an experiment.

There are three parts of an OSSE, (i) the nature run (NAT) that represents the "true" conditions of the aerosol state in the atmosphere, (ii) the control (CTL) run of the model, which sets the baseline performance of the model without data being assimilated, (iii) and the data assimilation run (DAS) where synthetic observations are assimilated in a model identical to the CTL model in order to improve aerosol emissions. The intercomparison of the differences between CTL and NAT and DAS and NAT can provide the added value of the assimilated observations, identify limitations of the data assimilation system, or quantify the role of some processes on the estimated emissions. The main goal of the present paper is to assess the ability of different satellite observations for quantifying aerosol emissions. Therefore, for all experiments we use the same physical model for the NAT, CTL, and DAS because otherwise we cannot attribute differences between NAT and DAS to either limitations of the satellite observations or model differences. We also perform some additional experiments with different nature runs (NAT_M, NAT_E) to assess different causes of uncertainty in emission estimation (e.g., biased meteorology) in addition to the standard nature run (NAT) and partially address the OSSE identical twin problem (Arnold and Dey, 1986; Timmermans et al., 2015). Note that the meteorology of all experiments is nudged to the ensemble mean of the 10 analysis members of

ERA5 (Hersbach et al., 2020), except the nature run NAT_M (details below).

The standard nature run (NAT) only changes the emissions in comparison to CTL, by multiplying the default emissions of DU and SS by 0.5; the default emissions of OC and BC by 2; and the default emission of SO_4, SO_2, and DMS by 1.5. These emission factors are within the current range of uncertainty of aerosol emissions (discussed in Tsikerdekis et al., 2021a) and create a distinct difference in the global and regional distribution of AOD, AE, and SSA in comparison to CTL. These emission factors are chosen arbitrary, aiming to test if the data assimilation is able to estimate them correctly (test the system), rather than to reduce biases between NAT and a specific set of observations of an existing satellite (e.g., POLDER-3). Nevertheless the differences between CTL and POLDER and CTL and NAT exhibit similarities in the biomass burning region in the tropics and the global ME and MAE of these differences are on the same scale (not shown). The second nature run (NAT_M) uses the same altered emissions as NAT but its meteorology is nudged to reanalysis ERA-Interim. Consequently, the assimilated observations sampled from NAT_M can show the impact of biased meteorology on emission estimation. To investigate whether the scaling of emissions in NAT represents a too simple difference between nature and data assimilation run, a new nature run (NAT_E) was performed that changes emission parameterizations schemes for DU and SS and uses different emission inventories for the other species. This approach creates distinct spatiotemporal differences between the two runs in each species. An overview of all the NAT emission choices is depicted in Table 1.

3.4 Instrument coverage and uncertainty

The SPEXone spatial coverage at native resolution ($\sim 5.4 \times 4.6$ km) was simulated using an orbit simulator for cloud-free pixels based on the MODIS cloud product. In our case, we would like for SPEXone spatial coverage to be consistent with ECHAM clouds; thus, we modified the SPEXone spatial coverage to match ECHAM cloud mask. The goal of this post-processing was to create an ECHAM cloud-based SPEXone mask that provided a similar amount of observations to that of the MODIS cloud-based SPEXone mask (more details are given in Appendix B).

An ideal sensor in terms of spatial coverage was assumed in order to test the data assimilation system and act as a benchmark for the SPEXone ability to estimate aerosol emissions. This sensor, hereafter referred to as SUPER, is able to retrieve AOD_{550}, $AE_{550–865}$, and SSA_{550} over the whole globe every 2 d. The 2 d global coverage was based on the step of the data assimilation set which estimates the emissions every 2 d. In addition, the SUPER sensor is able to get aerosol observations even over cloudy pixels and over very high latitudes.

The spatial coverage for a 2 d period for these two satellites is shown in Fig. 3. Note that SUPER has a fixed number of observations in time and space, while the number of SPEXone observations fluctuates in time and space depending on cloud cover and orbit characteristics. The total number of grid cell observations (each grid cell includes an AOD_{550}, $AE_{550–865}$, and SSA_{550} value) assimilated for the period 20 July to 20 September 2006 is more than double in SUPER (139 872) compared to SPEXone (61 086). The observations we are using are super-observations, meaning that all the high-resolution SPEXone observations were aggregated to the model resolution ($1.875° \times 1.875°$). At the original resolution of SPEXone, our SUPER sensor would provide approximately 6 times the observations. Note that in that case these observations would be very closed together and highly spatially correlated. In addition, with super-observations the swath of SPEXone appears larger than 100 km, since only one high-resolution SPEXone resolution within each grid box is needed to provide a value for the whole grid box of a size $1.875° \times 1.875°$ (~ 250 km).

An instrument and retrieval simulator was used to generate estimates of observational errors. Retrievals for 4 individual days were used for this purpose. To be more specific, the estimated uncertainty is based on the difference between the retrieved and the true values, following a similar method to that of Tsikerdekis et al. (2021a). More details can be found in Appendix C. Note that these observational uncertainties were used for both satellites (SUPER and SPEXone).

3.5 Experimental setup

All of the experiments span 2 months in the summer of 2006 (20 July to 20 September 2006). This year and period was chosen based on our previous work (Tsikerdekis et al., 2021a). Prior to this period the model was spun up for 3 months (1 April to 1 July 2006), and the ensemble background emissions were spun up for 20 d (1 July to 20 July 2006). We employ a grid resolution T63L31 ($1.875° \times 1.875°$, with 31 hybrid-sigma vertical layers concentrated in the troposphere).

There are a few LETKS parameters that can be adjusted. In this study we keep these parameters fixed in all of our experiments. The description, discussion, and sensitivity experiments of these parameters (ensemble size, inflation local patch size, and the horizontal localization) was presented in our preceding study (Tsikerdekis et al., 2021a). The data assimilation ensemble size consists of 32 members. The local patch size and the horizontal localization are set to eight and four grid cells, respectively, while the inflation is set to 1. The inflation parameter is essentially deactivated with the value equal to 1, since under the emissions estimation setup of the data assimilation system the background uncertainty remains large enough throughout the experiment for the data assimilation to work. The local patch size is deliberately chosen to

Table 1. Emissions inventories and schemes used per sector for all NAT experiments. Note that NAT and NAT_M use the same emissions inventories and schemes as CTL and DAS but use emission factors (per species) to scale the emissions. ACCMIP is the Atmospheric Chemistry and Climate Model Intercomparison. GFAS is the Global Fire Assimilation System. CEDS is the Community Emissions Data System. The terms ndust and nseasalt refer to the emission scheme options used by the model ECHAM-HAM.

Emission sectors	Species	CTL and DAS	NAT and NAT_M (emission factors)	NAT_E (schemes & inventories)
Dust	DU	ndust = 5	0.5	ndust = 2
Sea salt	SS	nseasalt = 7	0.5	nseasalt = 2
Oceanic	DMS	nseasalt = 7	1.5	nseasalt = 2
Forest fires	OC, BC, SO_2, DMS	GFAS	2 or 1.5	ACCMIP
Grass fires	OC, BC, SO_2, DMS	GFAS	2 or 1.5	ACCMIP
Domestic	BC, OC, SO_2	ACCMIP	2 or 1.5	CEDS
Energy	BC, OC, SO_2	ACCMIP	2 or 1.5	CEDS
Industry	BC, OC, SO_2	ACCMIP	2 or 1.5	CEDS
Ships	BC, OC, SO_2	ACCMIP	2 or 1.5	CEDS
Transport	BC, OC, SO_2	ACCMIP	2 or 1.5	CEDS
Waste	BC, OC, SO_2	ACCMIP	2 or 1.5	CEDS
Aircraft	BC	ACCMIP	2	CEDS
Agricultural waste burning	BC, OC, SO_2	ACCMIP	2 or 1.5	ACCMIP
Biogenic	OC	AEROCOM II	2	AEROCOM II
Terrestrial	DMS	AEROCOM II	1.5	AEROCOM II
Volcanic (continuous)	SO_2	AEROCOM II	1.5	AEROCOM II
Volcanic (explosive)	SO_2	AEROCOM II	1.5	AEROCOM II

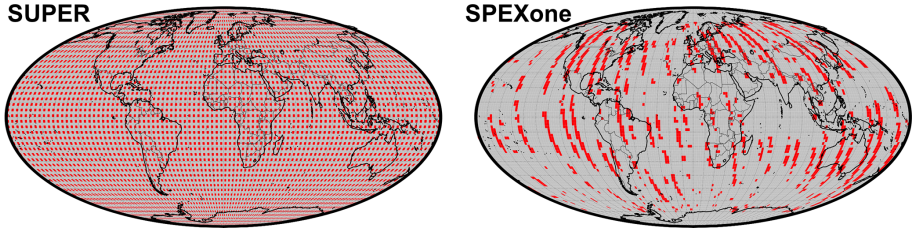

Figure 3. Red grid cells illustrate the 2 d spatial coverage of SUPER and SPEXone instruments. SPEXone coverage is shown for the 17 and 18 August. In both cases the observation size is $1.875^\circ \times 1.875^\circ$ (super-observations) and includes estimates of AOD_{550}, $AE_{550–865}$, and SSA_{550}.

be high (8) in order to let observations that are far away from the source (up to 15°) impact the emission estimation.

Table 2 shows the list of experiments related to SPEXone. The experiment where the assimilated observations are based on the SUPER spatiotemporal sampling is used mainly as a benchmark for the performance of the experiments that use the SPEXone sampling. The experiments where the assimilated observations use the SPEXone satellite coverage intend to evaluate the added value provided by the SPEXone instrument's ability to estimate emissions under different observational uncertainty and data assimilation options. Specifically, the experiment SPX used the default errors estimated for SPEXone retrievals (Appendix C). The experiment SPX_2U doubles the uncertainty of the assimilated observations, and SPX_2URE doubles the uncertainty and adds random errors (with standard deviation equal to the observational uncertainty) to the assimilated observations. Finally, SPX_W1 and SPX_W2 reduce the ΔT_a length to 4 and 2 d respectively (from 6 d originally); hence, fewer observations are used to derive the analysis emissions in each assimilation cycle and only one and two assimilation cycles (instead of three) are used to calculate the analysis emission perturbations. Consequently, the data assimilation experiment is faster and less computationally expensive, but fewer observations are used to obtain the analysis emission.

Sensor SUPER is further used in other sensitivity experiments that aim to assess issues related to the nature run complexity and development of the data assimilation system (Table 3). The SUP0_M experiment points out the degradation in emission estimation purely due to biased wind by assimilating observation from NAT_M. SUP_E assimilates observation from NAT_E and shows that even under totally different emission schemes and emission inventories between the nature run and the data assimilation experiment, the emission errors are reduced.

Table 2. List of experiments related to SPEXone.

Experiments	Satellite coverage	Satellite uncertainty	Add random error in observations	ΔT_a, ΔT_s	Comments
CTL	×	×	×	×	No data assimilation
SUP	SUPER	SPEXone	×	6, 2	Data assimilation based on SUPER sensor (benchmark performance of the filter)
SPX	SPEXone	SPEXone	×	6, 2	Data assimilation based on SPEXone sensor
SPX_2U	SPEXone	SPEXone · 2	×	6, 2	Data assimilation based on SPEXone sensor with double uncertainty
SPX_2URE	SPEXone	SPEXone · 2	✓	6, 2	Data assimilation based on SPEXone sensor with double uncertainty and added random errors to the observations
SPX_W1	SPEXone	SPEXone	×	4, 2	Data assimilation based on SPEXone sensor with shorter ΔT_a
SPX_W2	SPEXone	SPEXone	×	2, 2	Data assimilation based on SPEXone sensor with even shorter ΔT_a

Table 3. List of experiments related to other uncertainty factors that can affect emission estimation.

Experiments	Assimilated nature	Emission state vector	Prior correction	Comments
SUP0	NAT	by species	×	Tests the effect of prior correction
SUP0_M	NAT_M	by species	×	Tests the effect of biased meteorology
SUP_E1	NAT_E	by species	×	Tests the effect of realistic emission differences between nature and data assimilation runs
SUP_E2	NAT_E	by species	×	Tests the effect of realistic emission differences between nature and data assimilation runs and estimates emissions by mode for SS and DU
SUP_E	NAT_E	by species and mode	✓	Tests the effect of realistic emission differences between nature and data assimilation runs, estimates emissions by mode for SS and DU, and enables prior correction without the prior max flag

3.6 Data assimilation initialization

The prior emissions may be overestimated or underestimated, and the smoother (+ prior correction) will take time to adjust them. The smoother's time window of 6 d suggests that correct estimation of emissions does not happen until a multiple of that number of days has passed. During this period, the smoother is adjusting to the major biases present in the CTL emissions. We define this period based on the results of our data assimilation experiment in order to exclude it from the evaluation that follows in Sect. 4.

Figure 4 shows that the differences between DAS and NAT (solid lines) reach a value close to zero after 26 d. From that point until the end of the experiment, these differences fluctuate around zero. For comparison the emission differences of CTL–NAT (dashed lines) are also shown. Note that the day-to-day dust and sea salt emission differences can fluctuate a lot in CTL, but SUP is able to estimate them adequately.

The duration of the initialization phase may be expected to be a multiple of the longest of two timescales: the aerosol lifetime (that determines how quickly aerosol are deposited) and the DA window (that determines how quickly we can adjust emissions based on observations).

This is shown in Fig. 5, where after approximately 26 d the differences in aerosol optical properties and column burden relative differences between DAS and NAT reach a value close to zero and start fluctuating around this value until the end of the assimilation experiment. Consequently, we choose

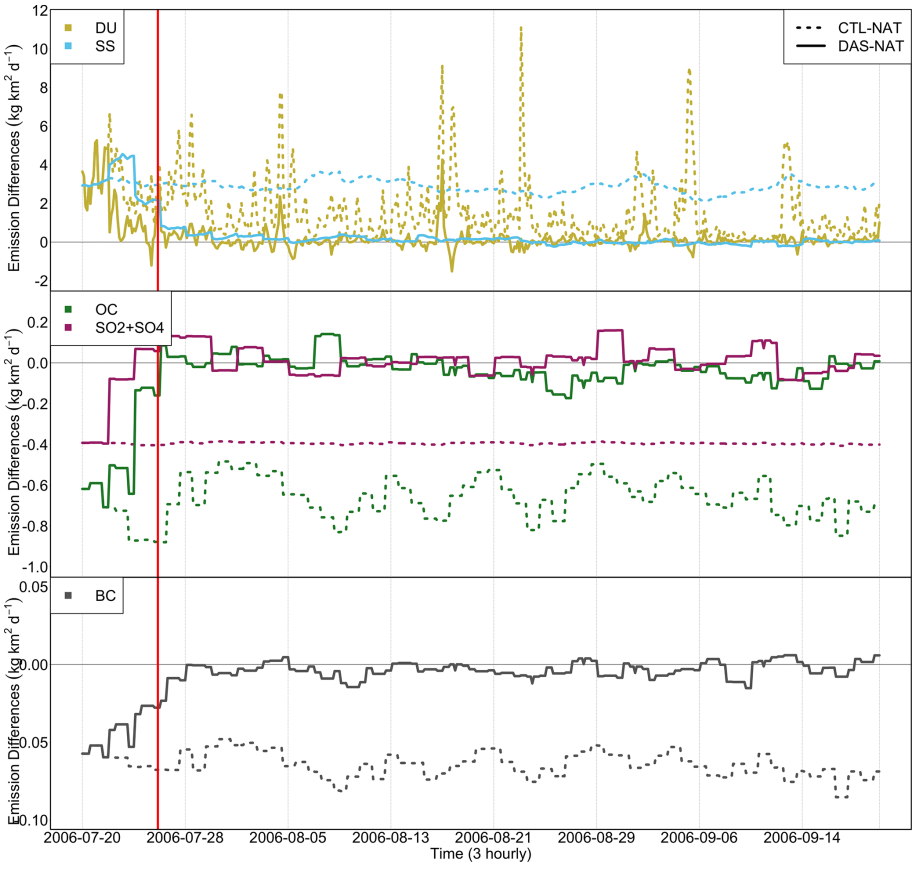

Figure 4. Time series for emission fluxes differences between CTL–NAT and SUP (DAS)–NAT for each species. The red line indicates where the analysis emissions perturbations were estimated for the first time. Note that SO_4 direct emissions are only a small fraction (2.5 %) of SO_2 emissions in ECHAM-HAM; hence, they are shown as a sum $SO_2 + SO_4$ in the plot.

the period of 26 d as the data assimilation initialization period, and only the remaining 36 d, spanning from 15 August 20 September 2006, are evaluated in Sect. 4. Note that the data assimilation initialization varies for each experiment depending on the amount of the assimilated observations, the differences with nature run, and the assimilation options used. Nevertheless, 26 d is sufficient as a data assimilation initialization period for all experiments (not shown) (except SUP_E for SS emissions in the coarse mode); thus, it is kept constant throughout the paper.

4 Results

4.1 Emission estimation using SPEXone

The ability to estimate the true aerosol state using SPEXone is compared to an experiment in which observations were assimilated based on a sensor like SPEXone (meaning that it can retrieve the same type of observations with the same accuracy) but with an almost perfect global coverage. In order to understand the simulated aerosol state for the examined period, the aerosol optical properties of the CTL experiment are shown and discussed in Fig. 6. High AOD is evident over Sahara and Arabian Peninsula mainly due to dust; over tropical forests (Amazon, Africa, Indonesia) mainly due to organic and black carbon; and over Europe, North America, and China mainly due to sulfates. AE is small over isolated ocean areas that are dominated by sea salt and shows high values over land, excluding desert areas where large dust particles prevail. High AAOD (low SSA) highlights high black carbon concentrations, either from natural (biomass burning) or anthropogenic (fossil fuel) sources, and intermediate values over high sources of dust. Note that SSA (not AAOD) is the quantity that is assimilated in our system (for details on the differences between SSA and AAOD assimilation, see Tsikerdekis et al., 2021a), but AAOD is shown in the plots since it is easier to interpret.

The ability of SPEXone and SUPER sensors to recreate the NAT are summarized in Fig. 7, where the differences between the experiments CTL, SUP, and SPX from NAT are depicted for AOD, AE, and AAOD. In both data assimilation experiments the modeled aerosol is improved when compared to the CTL experiment, and the global mean error (ME) and the global mean absolute error (MAE) are almost zero.

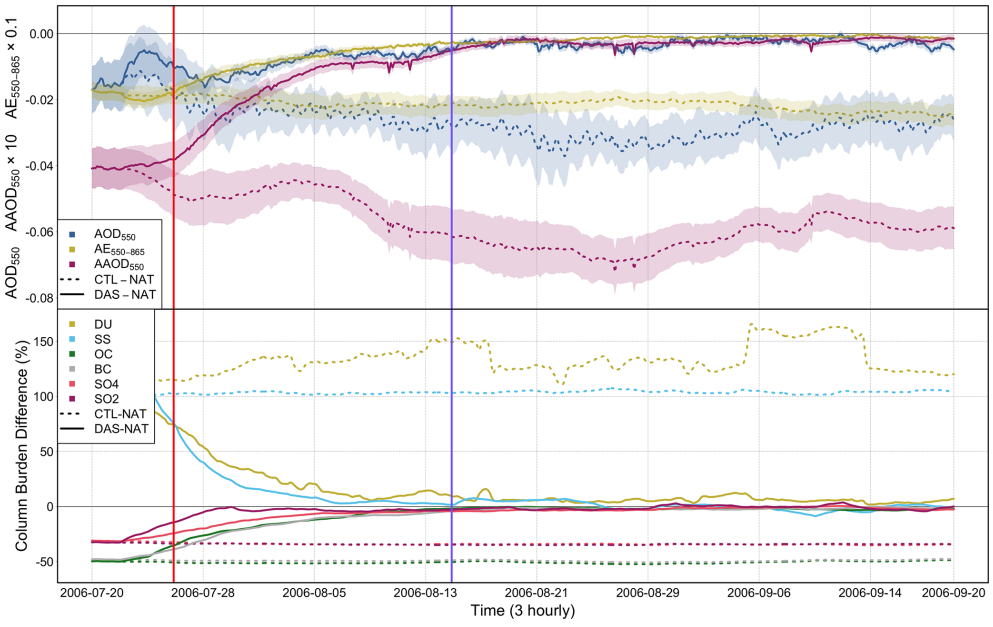

Figure 5. Time series of aerosol optical properties and column burden differences between CTL-NAT (dashed lines) and SUP (DAS)-NAT (solid lines). Column burden is depicted as relative differences. The vertical red line indicates when the analysis emissions perturbations were estimated for the first time, and the vertical purple line indicates when the plotted variables reach equilibrium with the analysis emissions. The period between the red and the purple lines indicates the lag time of the global aerosol burden's reaction to the analyzed emissions.

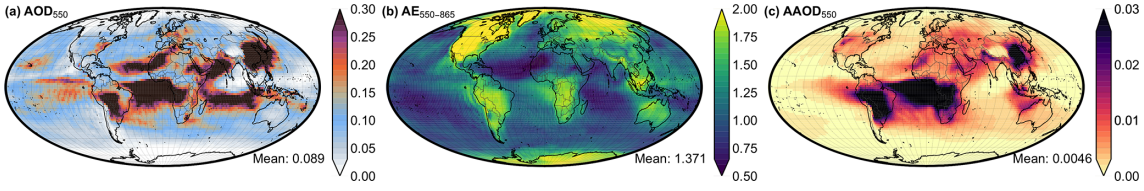

Figure 6. Aerosol optical properties for the CTL experiment. The mean stand for the global mean value is shown and is estimated by averaging all the available grid cells.

The ME and MAE equations can be found in Appendix B of our preceding publication (Tsikerdekis et al., 2021a). The performance of SPX is as good as the SUP, which suggests that the spatial coverage of SPEXone is sufficient to constrain the emissions in a similar fashion to the SUPER satellite.

An important advantage of OSSEs is that we are able to evaluate the estimated emissions of the data assimilation experiments with the emissions of the nature run. Figures 8 and 9 depict the emission of aerosol species for NAT and the emission differences for CTL, SUP, and SPX from NAT. In both data assimilation experiments the estimated emissions are improved compared to the emissions of the CTL. The overestimated dust emissions in the CTL are constrained in the data assimilation experiments, and the ME is not close to zero only in the western part of the Sahara desert where emissions are high. For both data assimilation experiments the relative ME averaged for the same region is lower than 10 % (not shown). The overestimated sea salt emissions in CTL are constrained globally in both data assimilation experiments, though in SPX the sea salt emission over the Indian Ocean shows high ME with relative ME in some grid cells that exceeds 50 %. This is caused by the limited observations by SPEXone due to cloudiness over India and the surrounding seas (see Fig. B2). The ME and the relative ME emission for organic and black carbon over high sources, mainly over the tropics in South America, Africa, and Indonesia but also over eastern China, reach almost zero in the data assimilation experiments. Sulfates in the model are mainly produced from SO_2 precursor emissions, and only a small fraction (2.5 %) of sulfates are directly emitted to the atmosphere. For all other species (DU, SS, OC and BC) the assimilated aerosol optical and microphysical observations directly constrain the emission of the particles that form these observations in the atmosphere. Despite that, the $SO_2 + SO_4$ emissions are constrained reasonably well, especially over high anthropogenic sources (North America, Europe, India, and China), where the relative ME per grid cell does not exceed 10 % (not shown) in both data assimilation experiments. These results

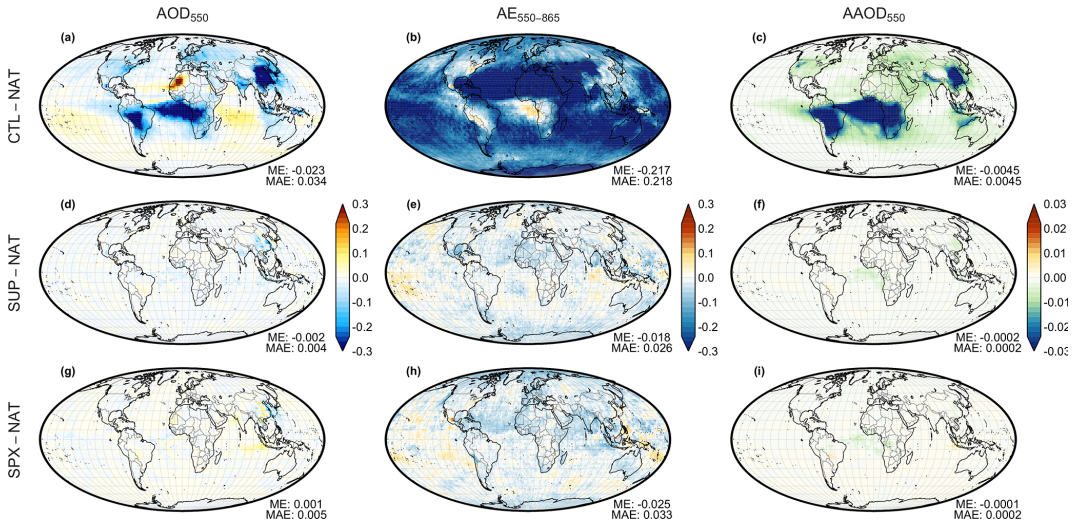

Figure 7. Differences in aerosol optical properties of CTL–NAT **(a, b, c)**, SUP–NAT **(d, e, f)** and SPX–NAT **(g, h, i)**. The left column depicts AOD **(a, d)**, the middle column depicts AE **(b, e)**, and the right column depicts AAOD **(c, f)**.

suggest that SPEXone limited observational coverage can estimate global aerosol emission in a similar manner to a sensor that would have an almost perfect observational coverage. However, it is noted that local error due to cloudiness deteriorates the performance of SPEXone in comparison to SUPER. Further, we assume that the 1.875° aggregate of SPEXone contains a non-significant representation error and that the observations of both sensors are unbiased.

4.2 Emission estimation using SPEXone – sensitivity experiments

A series of data assimilation experiments were conducted in order to explore less optimistic (SPX_2U) scenarios for the SPEXone retrievals and also to check what the effect is of adding actual noise to the observations (SPX_2URE) instead of relying purely on the uncertainty descriptions of the measurements. Further, we vary the ΔT_a length (SPX_W1, SPX_W2) of the data assimilation system. The differences of these two data assimilation experiments from NAT for AOD, AE, and AAOD are depicted in Fig. 10. In all cases the observations improve compared to the CTL experiment (Fig. 7a–c), although not to the extent of the default experiment SPX, which was discussed in the previous subsection (Fig. 7g–i).

Specifically, SPX_2U, where the assimilated observation uncertainty was doubled, shows similar results for AOD and AE, whereas the AAOD bias is increased slightly in comparison to SPX (Fig. 10a–c). SPX_2URE, where the assimilated observations uncertainty was doubled and random errors (with standard deviation equal to the observational uncertainty) were added to the assimilated observations, the bias increases over northeastern China for AOD, over the Sahara, Arabian Peninsula, and northern Indian ocean for AE, and over tropical Africa and the Amazon basin for AAOD (Fig. 10d–f). We can quantify the effect of an observation's random error on emission estimations by comparing the experiments SPX_2U and SPX_2URE. The data assimilation performance does not degrade significantly when taking into account random errors in the assimilated observations. Specifically the dust emission global MAE increases by 5 percentage points due to random errors, while for other species the increase is even lower (Fig. 13).

SPX_W1 and SPX_W2 reduce the ΔT_a length to 4 and 2 d (from 6); hence, fewer observations are used to derive the analysis emissions in each assimilation cycle, and only one and two assimilation cycles (instead of three) are used to calculate the analysis emission perturbations. The results reveal that $\Delta T_a = 4$ d (SPX_W1) is sufficient to constrain the AOD, AE, and AAOD in a similar manner to $\Delta T_a = 6$ d (SPX) (Fig. 11a, b, c). In other words, under the current experimental setup, observations 5 to 6 d after the emissions probably hold very little information for the correction of these emissions, and their exclusion has a very limited impact on the data assimilation performance. In contrast, the experiment SPX_W2 shows a degradation in performance over the western Sahara and northern Atlantic for AOD and AE (Fig. 11d, e, f), indicating that observations during the subsequent days 3 and 4 hold useful information for the correct estimation of emissions at day 1 and 2, as will be discussed below. Note that SPX_W1 and SPX_W2 need $\sim 33\,\%$ and $\sim 66\,\%$ fewer computational resources than SPX, respectively, since the background step in each assimilation cycle is shorter.

Figure 12 shows the mean and standard deviation of errors per grid cell. These errors are averages for the evaluation period of the difference between an experiment (CTL or DAS) and NAT. Both SUP and SPX errors are significantly smaller than CTL in both global (mean) and local errors (spread). The global AOD MAE of SPX_2U and SPEX_2URE re-

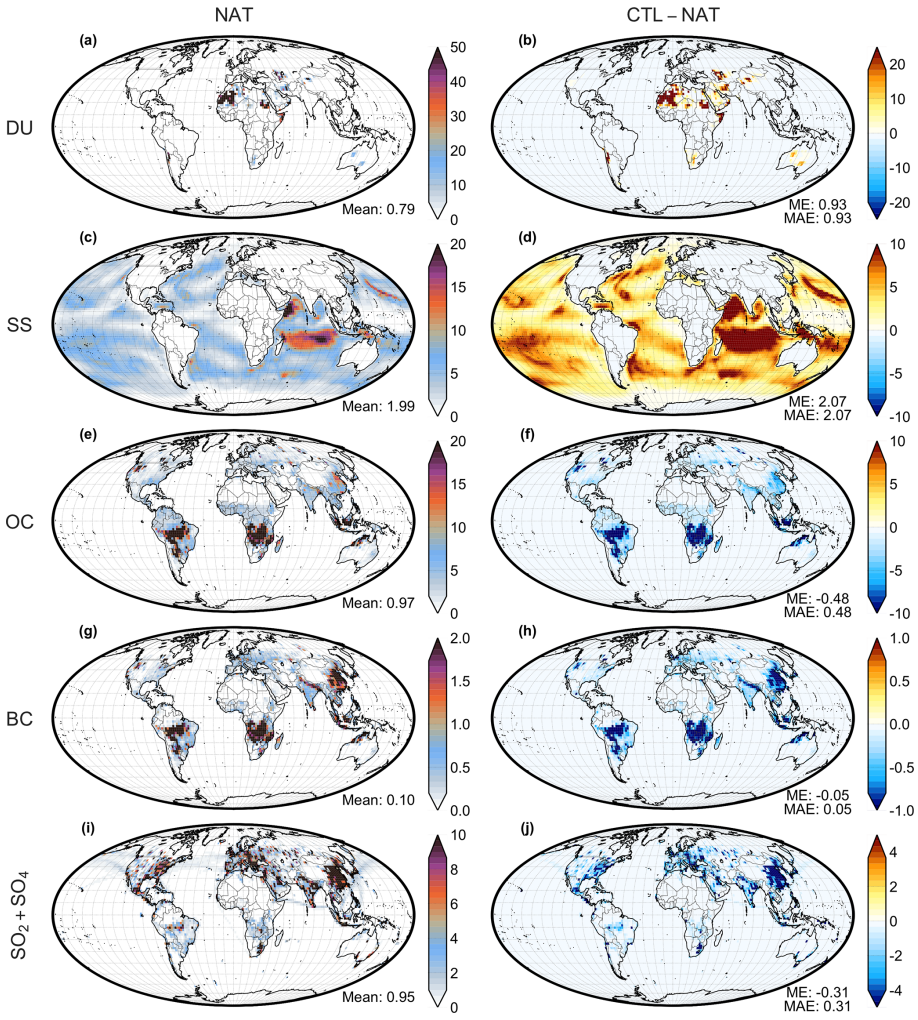

Figure 8. Aerosol emission fluxes ($\mathrm{kg\,km^{-2}\,d^{-1}}$) for NAT by species: **(a)** DU, **(b)** SS, **(c)** OC, **(d)** BC, and **(e)** $SO_2 + SO_4$. The second column depicts the differences between CTL and NAT.

mains very low, while AE and AAOD global ME slightly increase. Note that SPEXone AOD uncertainty range (Appendix C) is very low (lower than 10 % over ocean and 15 % on average over land), and doubling this uncertainty only has a limited effect on the analysis. On the other hand, the uncertainty in AE and SSA observations is higher than AOD; hence, the data assimilation performance is affected to a larger extent. Overall, it can be concluded that in these less optimistic assessments (doubled uncertainty), the assimilated observations based on SPEXone spatial coverage are still able to estimate the emissions with reasonable accuracy. Further, the experiment where actual noise is added to the measurements shows similar results to the experiment where no noise was added. This illustrates that the system is not "overfitting" the observations but takes the specified uncertainty correctly into account even when there is no noise added to the measurements.

In terms of estimated emissions, the four sensitivity experiments rank a bit lower in comparison to both SUP and SPX, as indicated in Fig. 13, where the global relative MAE for various species is shown. Specifically, SPX has similar emission errors to SUP but differs in the SS-estimated emission, which is caused by the limited observations in SPEXone due to cloudiness over India and surrounding seas (see Fig. B2), as discussed in the previous subsection. SPX_2U and SPX_2URE emission biases for all species are increased by no more than 10 percentage points in comparison to SPX, which indicates that increased (double) uncertainty and adding random errors in the observations has a small but noticeable negative effect on the global relative differences in the emissions. Finally, SPX_W1 emission bias increases by no more than 6 percentage points in comparison to SPX in all species. However, dust emission error grows to 54 % in SPX_W2 from 17 % in SPX_W1, indicating that the information content of observations 3 and 4 d after the emissions

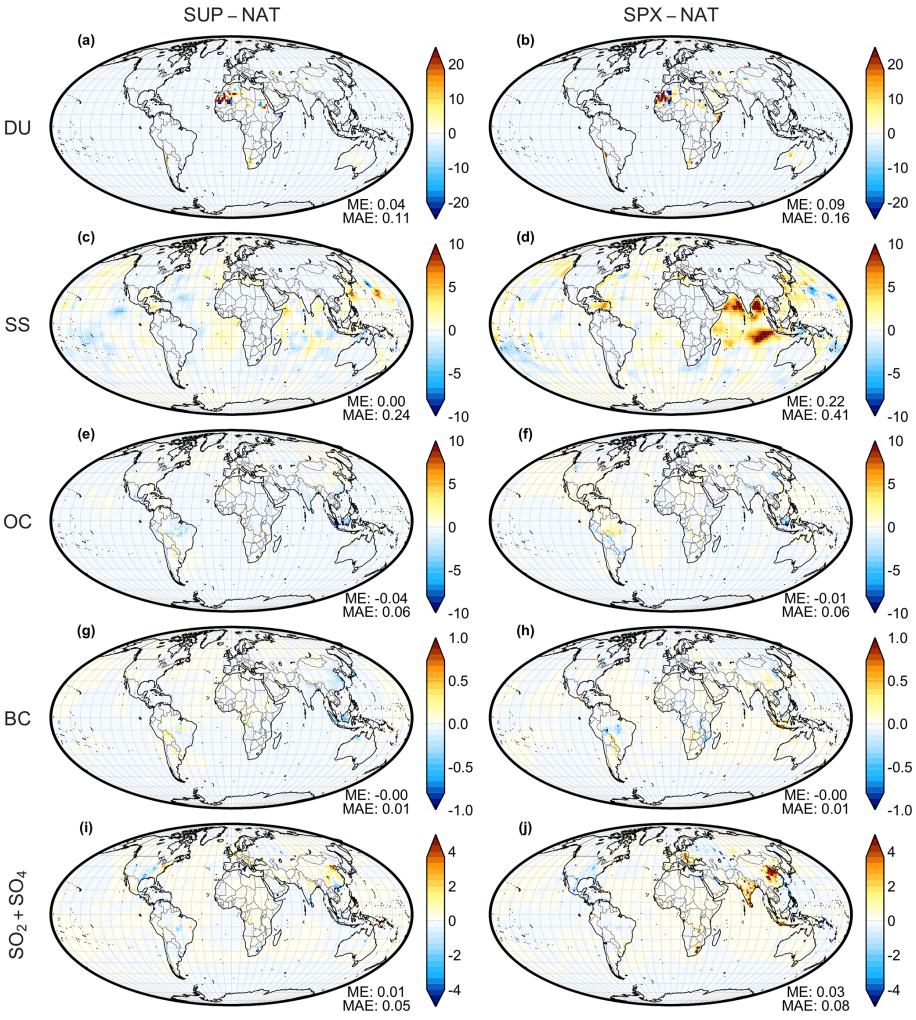

Figure 9. The same as Fig. 8 but for the differences between SUP and NAT and SPX and NAT.

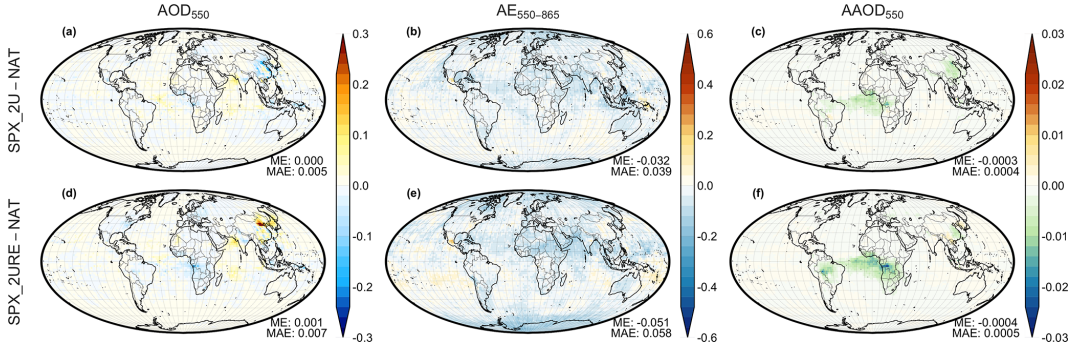

Figure 10. Differences in aerosol optical properties between SPX_2U and NAT **(a, b, c)** and SPX_2URE and NAT **(d, e, f)**. The left column depicts AOD **(a, d)**, the middle column depicts AE **(b, e)**, and the right column depicts AAOD **(c, f)**.

is very rich and should be used to correct these emissions, especially for Saharan dust plumes that extend over the Atlantic Ocean and last for several days. The emissions of OC, BC, and $SO_2 + SO_4$ are estimated very accurately by all of the data assimilation experiments, with relative MAE ranging from 0 % to 5 %, which indicates that, in terms of the global mean emission estimation, these emissions are unaffected by the sensor spatial coverages and observational uncertainty increases that were tested. The global maps of emission differ-

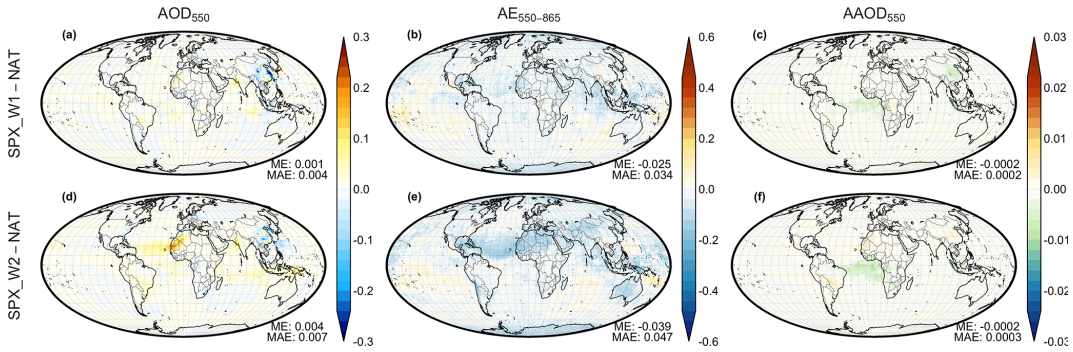

Figure 11. Differences in aerosol optical properties between SPX_W1 and NAT **(a, b, c)** and SPX_W2 and NAT **(d, e, f)**. The left column depicts AOD **(a, d)**, the middle column depicts AE **(b, e)**, and the right column depicts AAOD **(c, f)**.

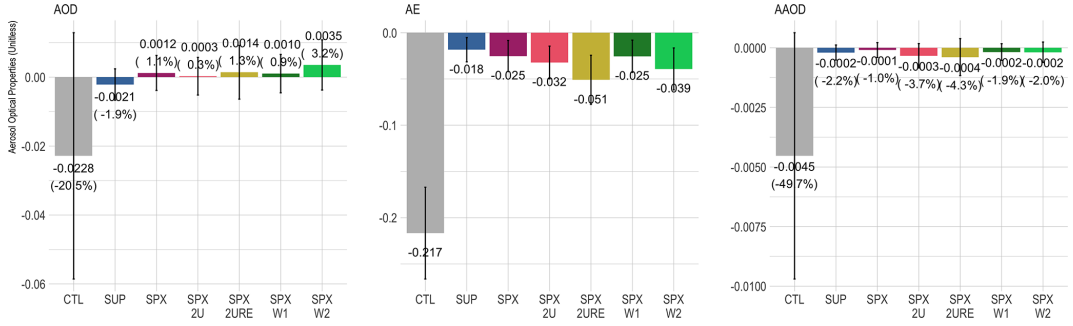

Figure 12. Global mean differences between CTL and several data assimilation experiments from NAT. Information in parentheses indicates the global mean relative difference. The error bar indicates the standard deviation of differences by grid for the whole globe. A larger (smaller) error bar indicates that local differences are higher (lower).

ences from NAT for the four sensitivity experiments of these subsection are shown in Fig. S1.

4.3 Other sources of uncertainty for emission estimation

OSSEs also allow us to quantify the uncertainty due to assumptions in nudging meteorology or emission source locations. The first relates to the assumption that the meteorological parts of the model and specifically the wind components (U and V) are perfect. The second factor relates to complex spatiotemporal change of aerosol emission in the nature run compare to the data assimilation run and test if the system is able to estimate the correct emissions when the data assimilation and nature runs emissions differ by more than just an emission factor (per species) that is constant in time and space.

4.3.1 The effect of biased meteorology

The OSSEs in previous subsections implicitly assumed that the data assimilation experiment would have perfect knowledge of the NAT meteorology. Since even reanalysis datasets of wind speeds have errors, we test their impact here. Simulations that were nudged to different reanalysis datasets (e.g., ERA-Interim and ERA-5) reveal very dissimilar results in terms of AOD, AE, and SSA for specific regions (Fig. 14g, h, i).

In this subsection we explore the effect of biased meteorology in the aerosol emission estimation by nudging the wind components of the nature run (NAT_M) to ERA-Interim and the wind components of the data assimilation (SUP0_M) experiment to ERA-5. The sampled observations of NAT_M are based on the SUPER sensor; hence, the observational coverage is optimal in space and continuous in time. Note that the emissions of NAT_M are scaled with the same scale factor as NAT (Table 1). Further, prior correction is not used in SUP0_M.

The evaluation of SUP0_M modeled aerosol against NAT_M reveals high errors in some regions (Fig. 14d, e, f). Unsurprisingly, AOD differences between SUP0_M and NAT_M and NAT and NAT_M shown in Fig. 14 display striking similarities for subtropical and tropical Africa and the Atlantic Ocean, as well as over East China Sea and Philippine Sea, which suggests that the remaining aerosol biases on SUP0_M are mostly related to the biased meteorology that affects aerosol transport paths.

In terms of the estimated emissions, SS is negatively affected the most by the effect of biased meteorology. Fig-

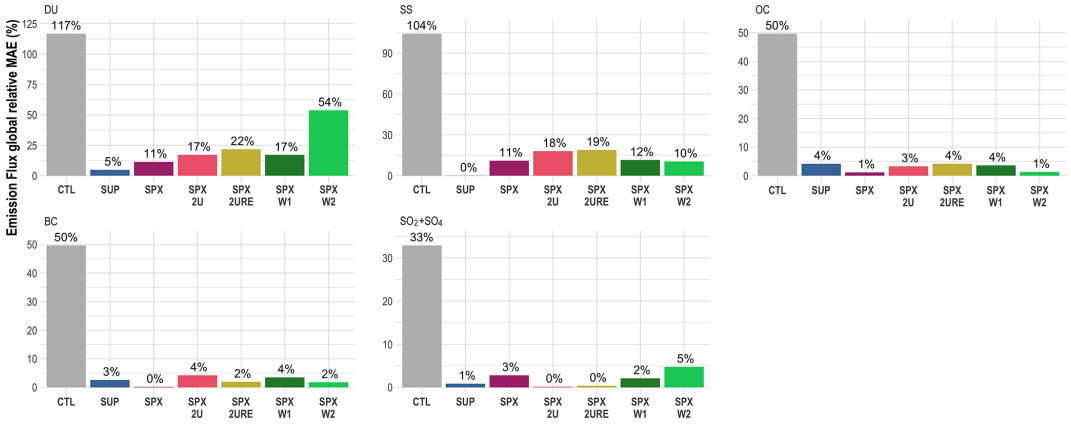

Figure 13. Global relative MAE (%) of species-specific emission fluxes for several experiments.

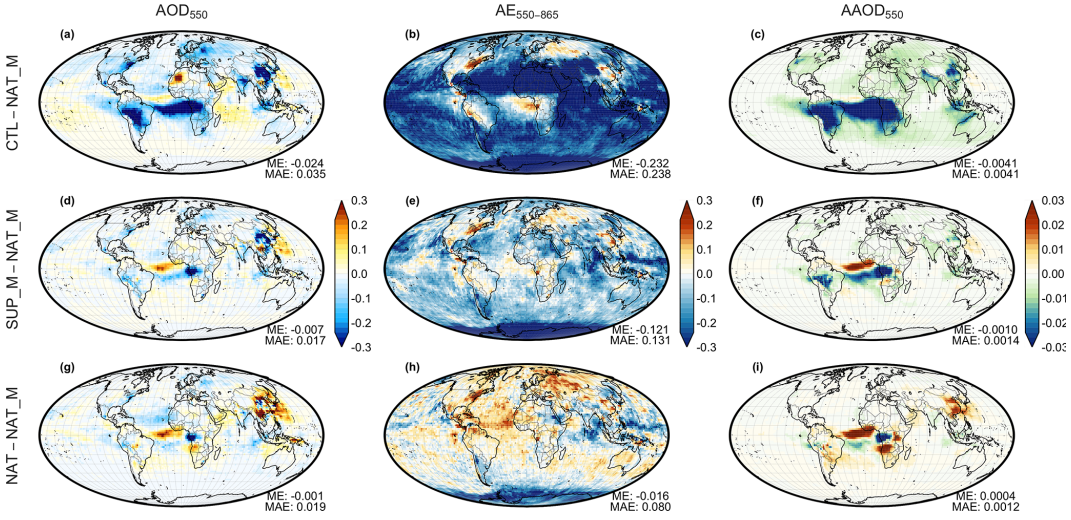

Figure 14. Differences in aerosol optical properties between CTL and NAT_M **(a, b, c)**, SUP_M and NAT_M **(d, e, f)**, and NAT and NAT_M **(g, h, i)**. The left column depicts AOD **(a, d, g)**, the middle column depicts AE **(b, e, h)**, and the right column depicts AAOD **(c, f, i)**. Note that the differences in the bottom row indicate changes in aerosol optical properties that are solely due to different meteorology.

ure 15 shows that the relative MAE in SS emissions increases by 24 percentage points in SUP0_M (42 %) compared to SUP0 (18 %), while the estimated emissions of DU, OC, BC, and $SO_4 + SO_2$ are negatively affected by the effect of biased meteorology to a smaller extent (~ 10 %). In addition, the comparison of the two grey bars, CTL (NAT) and CTL (NAT_M), shows that the different meteorology significantly changes the DU emissions and to a lesser extent the SS emissions. Note that regional error (estimated for each grid cell) can be higher than what is indicated in Fig. 15. The global map emission differences between CTL and NAT_M, SUP0_M and NAT_M, and NAT and NAT_M are shown in (Fig. S2).

Transport deviations (vertically and horizontally) between ERA-5 and ERA-Interim were assessed using Lagrangian transport simulations by Hoffmann et al. (2019). In that study differences of Lagrangian simulations based on the two reanalysis products were up to 2 to 3 orders of magnitude compared to differences caused by parameterized diffusion and subgrid-scale wind fluctuation after 10 d. Some of the main simulation improvements of ERA-5 compared to ERA-Interim are its higher spatial (31 km) and temporal (hourly analysis) resolution as well as its 4D-Var uncertainty estimate, which comes from a 10-member ensemble of data assimilation in a coarser resolution (63 km). Considering the improvements of ERA-5 compared to its predecessor, we assume that the aerosol differences (Fig. 14g, h, i) caused by nudging ECHAM-HAM to ERA-5 or ERA-interim represent a worst-case scenario and that the differences between ERA-5 and the real wind are not greater than that scenario.

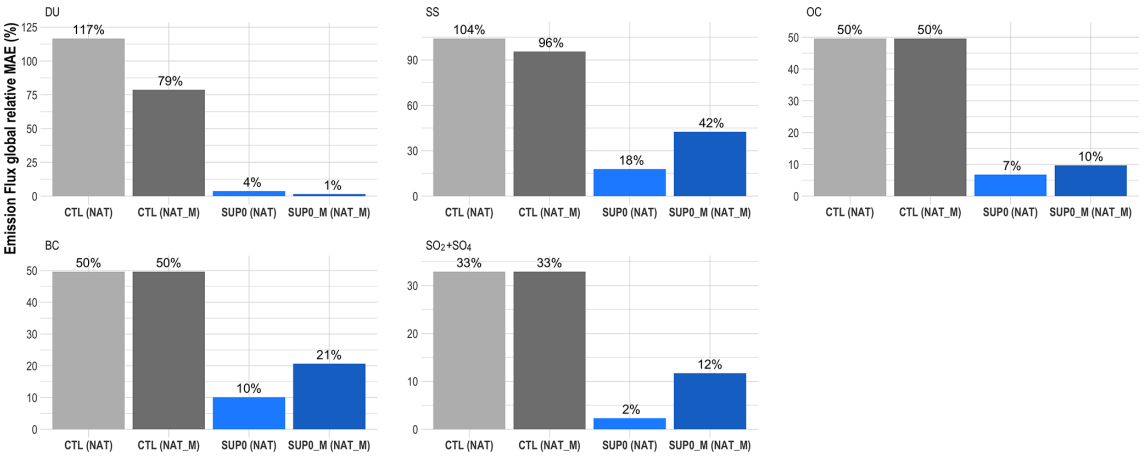

Figure 15. Global relative MAE (%) of species-specific emission fluxes for several experiments. The information in parentheses indicates the nature run, which is used as a reference in each case.

4.3.2 The effect of using different emission inventories between the nature and data assimilation runs

Our nature run (NAT) has emissions that are simply scaled for the different species compared to the control and data assimilation runs. To investigate whether this scaling represents a too simple difference between nature and data assimilation run, we conduct OSSEs with a new nature run (NAT_E). In this new nature run we change the emission inventories and emission schemes (Table 1) compared to the control and data assimilation runs. This creates a more realistic emission differences between NAT_E and CTL that fluctuate in time and space. The CTL to NAT_E differences in Fig. 16 illustrate an overestimation of AOD and AAOD over the tropics in South America and Africa. An underestimation of AOD is apparent in Southeast Asia and over the deserts in the western Sahara and Taklamakan. In addition, a strong global overestimation (0.46) of AE, mainly over the ocean, is observed due to a high amount of SS coarse particles emitted by the scheme selected in NAT_E.

In a new assimilation experiment (SUP_E) we used some new options. Emission estimation was conducted by mode and not only by species (separately for accumulation and coarse) for the SS and DU aerosol species. In addition, prior correction was used (without the prior max option). Both of these changes were introduced for the SUP_E experiment in order to create more variation in AE and let emissions of SS in the coarse mode match those in NAT_E, which are much higher than the background uncertainty for midlatitudes and high latitudes. Results of the data assimilation experiments, where we applied these two changes one at a time, are shown in Fig. S3.

In SUP_E, we perform a data assimilation experiment using the CTL baseline prior emissions with observations drawn from NAT_E. The data assimilation system was able to adjust model emissions in order to match the observations of NAT_E. Specifically, the global ME for SUP_E is zero for AOD and AAOD, while AE global ME is reduced from 0.46 to 0.11 (Fig. 16), with the highest local errors still persisting over high latitudes (Fig. S4 and explanation in caption).

The global relative MAEs for emissions are depicted by species in Fig. 17 for SUP_E and CTL. The emission errors of SUP_E for all species are reduced or remain almost unchanged ($SO_4 + SO_2$) compared to CTL. Although NAT_E uses very different emission inventories compared to SUP_E, the data assimilation system accurately fits the measurements and estimated (most) emissions correctly. The emission differences maps per species between CTL and NAT_E and SUP_E and NAT_E are depicted Fig. S5.

We focus on the Sahara region and the estimated DU emissions to highlight an important issue of any data assimilation system for emission estimation. Figure 18 depicts the dust emission fluxes over the western Sahara for the NAT_E, CTL, and SUP_E. Although the dust emission fields are similar, the spatial distribution of the dust sources differs. There are some grid cells where dust emissions are zero (not considered as sources by the model) in the control and the data assimilation experiment (highlighted with the red polygon at Fig. 18d), while the same locations are active sources in the nature run. These differences are caused by the setup of each dust scheme, where the preferential dust sources can differ (Schepanski et al., 2007). These contrasting assumptions can negatively impact the estimated emissions, since our data assimilation setup adjusts existing sources and does not introduce new sources. Dust emission differences between CTL and NAT_E (Fig. 18d) show an underestimation over these grid cells and the surrounding area in question. Differences between SUP_E and NAT_E (Fig. 18e) reveal that dust emissions remained underestimated over the same grid cells but that the surrounding emissions (especially westward) were increased (overestimated) to compensate for the lack of dust in the area. Hence, the data assimilation system not only un-

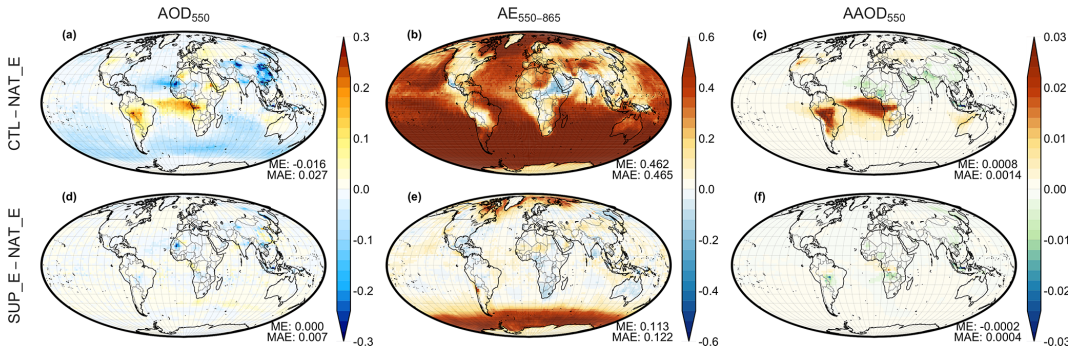

Figure 16. Differences in aerosol optical properties between CTL and NAT_E **(a, b, c)** and SUP_E and NAT_E **(d, e, f)**. The left column depicts AOD **(a, d)**, the middle column depicts AE **(b, e)**, and the right column depicts AAOD **(c, f)**.

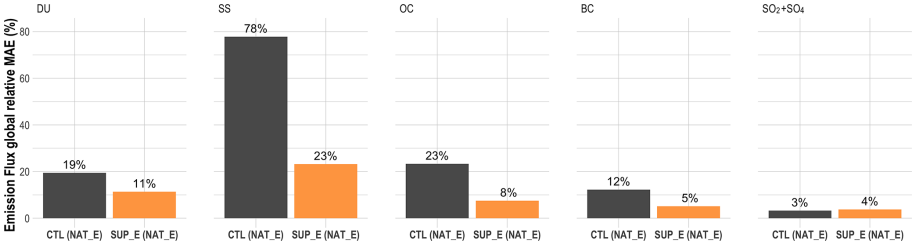

Figure 17. Global relative MAE (%) of species-specific emission fluxes for several experiments. The information in parentheses indicates the nature run, which is used as a reference in each case. Note that statistics were calculated for sources that are active on NAT_E.

derestimated these specific grid cells but ended up overestimating all of the surrounding area as well in order to compensate for the missing aerosol in the atmosphere. On the other hand, for emissions in areas where the location of preferential dust emission sources is the same, data assimilation did not have a problem estimating the correct emissions (highlighted with the orange polygon at Fig. 18c). These examples show that it is possible for a data assimilation system to reduce source strengths in the model, whereas it is not possible (under the current dust scheme and data assimilation setup) to start emitting dust in grid cells specified as non-sources. Consequently, dust schemes with spatially broader and continuous sources may provide a more flexible way to adjust the emissions based on observations. Note that although these examples reside in the modeling world of an OSSE, the same problem can affect the dust emission estimation of non-OSSE data assimilation studies since source location in models can differ from the source location in nature.

5 Conclusions

In this study we have quantified SPEXone ability to estimate aerosol emissions using a fixed-lag ensemble Kalman smoother (LETKS) in combination with the ECHAM-HAM aerosol–climate model. SPEXone is a passive remote sensing multi-angle polarimeter part of the NASA PACE missions scheduled to be launched in 2023. The system is tested using observing system simulation experiments where the nature run is created by an ECHAM-HAM simulation with altered aerosol emissions from the standard model setup. Synthetic observations of aerosol optical depth, Ångström exponent, and single-scattering albedo are sampled from this nature run according to the spatiotemporal coverage of SPEXone or a theoretical sensor with almost perfect global coverage.

The data assimilation experiments based on SPEXone or the theoretical sensor provide similar results in terms of the estimated emissions and the simulated observations, which is very encouraging since it shows that spatially limited SPEXone observational coverage will be able to constrain emissions almost as well as the theoretical satellite setup. Note that we assume that the 1.875° aggregate of SPEXone contains a non-significant representation error, the observations of both sensors are unbiased, and the differences in observations of the nature run and the data assimilation run are only caused by differences in emissions. We address most of these assumptions by conducting additional experiments.

Specifically, the initial global prior emissions errors in the control run that ranged from 33 % to 117 % (depending on the species) drop to a range of 0 % to 5 % for the theoretical sensor and 0 % to 11 % for SPEXone. The highest difference between the two sensors is observed on the SS-estimated emissions mainly due to the lack of observations for SPEXone over India caused by cloudy conditions. An observational uncertainty scenario for SPEXone that doubles the un-

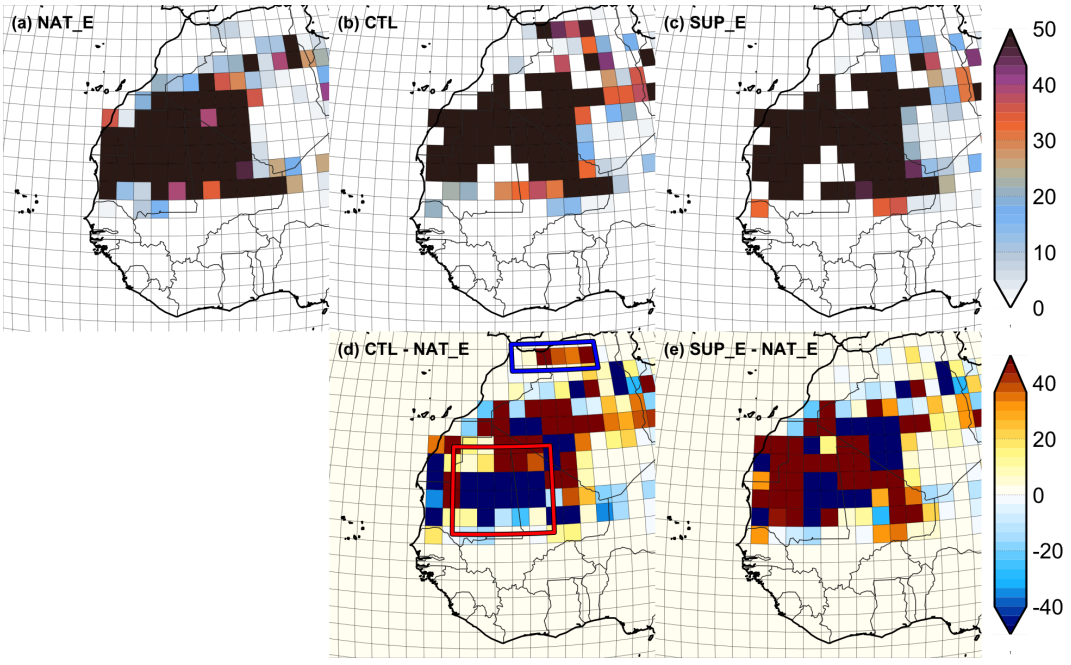

Figure 18. Dust emission fluxes (kg km^{-2} d^{-1}) for **(a)** the NAT_E, **(b)** the CTL, and **(c)** the SUP_E. The differences between CTL and NAT_E and SUP_E and NAT_E are depicted in panels **(d)** and **(e)**, respectively. Note that NAT_E uses a different dust scheme than CTL and SUP_E, hence the location where dust can be emitted differs. In subplot **(d)**, blue and red boxes highlight regions where dust emissions are overestimated and underestimated, respectively, in CTL compared to NAT_E. In the first case the data assimilation can modify the emissions and correct the overestimation, while in the second case it cannot (details in the Sect. 4.3.2).

certainty of the assimilated observations leads to reasonably good emission estimates. Further, we show the information of observations on days 5 and 6 after emission is not that important for the estimation of emissions (for all species), but the information of observations on days 3 and 4 after dust emissions is very important and should be used for the estimation of dust emissions. Note that in all of these experiments the nature run was created using the same model and the same physics options as the data assimilation run, with their only difference being that the emissions of the nature run were multiplied with emission factors that are globally constant and distinct for each aerosol species. Hence, the results of these data assimilation experiments may be too optimistic, since they do not account for any other uncertainty factor that would affect emissions estimation (e.g., meteorology biases, complexity in emission sources) in reality.

Therefore, additional experiments were conducted using the theoretical sensor in order to quantify the impact of other uncertainty factors that can affect the estimation of aerosol emissions. The role of biased meteorology is tested by nudging the wind components of the nature run to ERA-interim and the data assimilation run to ERA-5. Biased meteorology mostly increases global error in sea salt emissions in comparison to the data assimilation experiment where meteorology was not biased. The estimated emissions of the other species are negatively affected to a smaller extent.

Further, to investigate whether the creation of a nature run with emission scaling represents a too simple difference between nature and data assimilation run, an experiment where emissions in a new nature run are altered by changing the emission inventories and emission schemes. Data assimilation successfully reduced the global emission errors of all species, with the exception of dust at some locations. Dust emission errors are not reduced because the preferential dust sources of the nature run are greater compared to the data assimilation run. This complicates the emission estimation since dust is emitted from different locations in the nature run and the data assimilation run. Specifically, in the western Sahara data assimilation increases dust emission extensively in its available dust sources based on the assimilated observations (sampled from the nature run) in order to compensate for the lack of dust that originated from dust sources only available in the nature run. This OSSE demonstrates that a data assimilation system may not provide the desirable results in cases where the locations of emission sources are more sparse than nature.

This work highlights that the upcoming SPEXone sensor will provide high-accuracy observations with sufficient coverage that contains information about the mass, size, and absorption of the aerosol particles in order to estimate aerosol emission accurately using our data assimilation system. Using the full observational information of the PACE mission (SPEXone, HARP-2 and OCI), as well as using more re-

trieved aerosol properties (effective radius, refractive index), can potentially provide even better results.

Appendix A: The effect of prior correction

The Kalman filter assumes that the emissions do not have persistent errors or, in other words, that the emissions are not constantly biased (low or high) in time. Unfortunately, emissions in models can be biased; hence, we developed a prior correction method to account for this phenomenon. The effect of prior correction is tested by comparing the performance of the experiments with (SUP) and without (SUP0) prior correction. The simulated aerosols in the SUP0 experiment become almost identical to NAT, although a small bias remained in all variables (Fig. A1). This is due to the setup of our OSSE, where the prior emissions of all the species are biased either low or high in comparison to NAT. In other words, although the uncertainty of prior emissions describe the prior emission errors well, the biased prior ensemble mean has a small toll on data assimilation performance. With prior correction (SUP) this issue is resolved, and we get a better fit to the observations for all variables as shown in Fig. A1. The global error of the estimated emission is improved due to prior correction by 18 % for SS and by up to 7 % for the other species (not shown). Although the effect of prior correction is small for SUP and SUP0, in the case where the prior emissions error differs a lot from the uncertainty of prior emissions, the effect of prior correction would be much more significant, since it will adjust the ensemble mean of the emission perturbations and correct the bias of the model. An example of this is presented in Sect. 4.3.2 for the estimate of SS emissions.

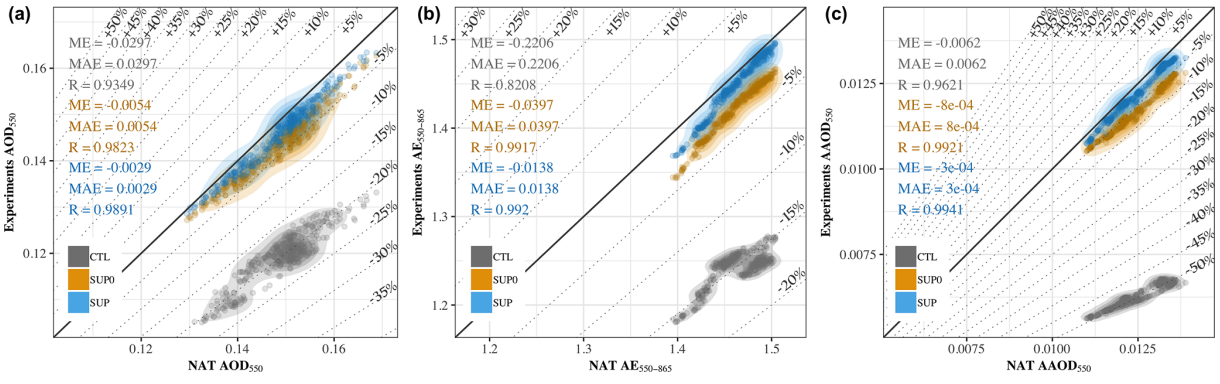

Figure A1. AOD_{550} **(a)**, $AE_{550–865}$ **(b)**, and $AAOD_{550}$ **(c)** scatterplot for the NAT, SUP, and SUP0 experiments. Each point represents a 3-hourly global mean. ME stands for mean error, MAE stands for mean absolute error and *R* represents the Pearson's correlation. The shaded areas represents the 2D kernel density estimation for each experiment.

Appendix B: SPEXone coverage based on a realistic ECHAM-HAM cloud mask

We want a realistic cloud mask that is nevertheless determined from the ECHAM cloud mask. The way we achieve this is by setting an ECHAM cloud fraction threshold for all the grid cells that coincide with the cloud-free SPEXone spatiotemporal coverage. When ECHAM cloud fraction of a grid cell is lower than the cloud fraction threshold, we assume that at least some observations could be retrieved over the cloud-free part of that grid cell. In order to make our results more realistic, we further change the cloud fraction threshold in each grid cell (in a statistical sense, by random draws) to make it appear more like MODIS cloud mask.

Specifically, the grid cells of the cloud-free SPEXone mask were filtered out based on ECHAM cloud fraction greater than 0.7 (ECHAM-CloudMask1 red points in Fig. B1). Although ECHAM and MODIS cloud-based SPEXone masks almost matched in the total number of observations, they differed in the latitudinal and temporal distribution of observations (especially at high latitudes and the subtropics) (black and red points in Fig. B1). Thus, we allowed the 0.7 cloud fraction threshold to change depending on how much the ECHAM and MODIS cloud-based SPEXone masks differ per latitude and time. This resulted in a SPEXone mask based on ECHAM cloud fraction but with the more realistic sampling that MODIS provides, specifically regarding time (ECHAM-CloudMask2 blue points in Fig. B1). The total number of observations retrieved by SPEXone based on MODIS and ECHAM cloud masks is depicted in Fig. B2.

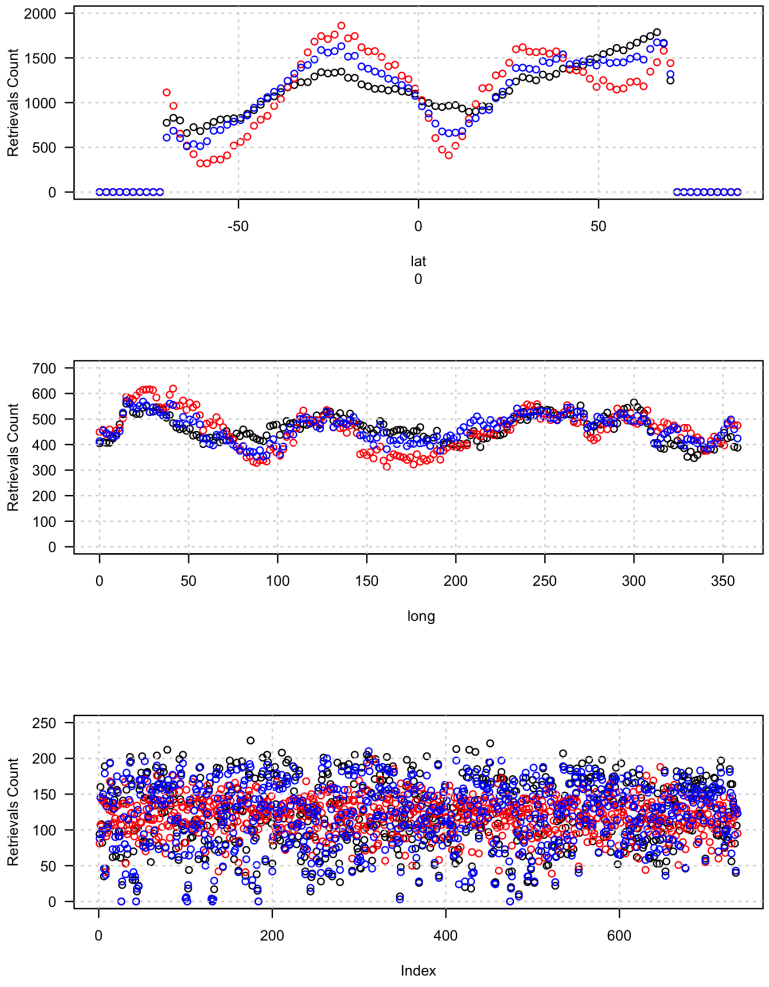

Figure B1. Number of observations by latitude, longitude, and time for the SPEXone mask based on MODIS cloudiness (black; MODIS-CloudMask), ECHAM cloud fraction <0.7 (red; ECHAM-CloudMask0), and ECHAM cloud fraction hybrid method explained in text (blue; ECHAM-CloudMask). The total number of observations for each mask is 88 731 for MODIS-CloudMask, 88 005 for ECHAM-CloudMask0, and 88 886 for ECHAM-CloudMask. The analysis refers to the period from 2 July to 1 October.

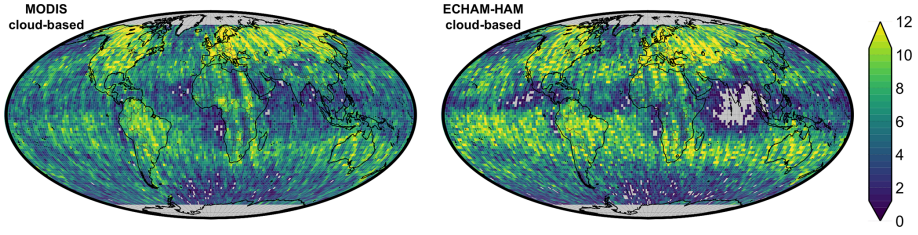

Figure B2. Number of observations for the MODIS and ECHAM-HAM cloud-based SPEXone masks. Each gridded observation includes an AOD_{550}, $AE_{550–865}$, and SSA_{550} measurement. The analysis refers to the period from 2 July to 1 October.

Appendix C: Observation uncertainty

We need to estimate the observational uncertainty for SPEXone, which is a sensor that is not yet launched. The retrievals errors of SPEXone are simulated as in Hasekamp et al. (2019a). The uncertainty of the retrieved parameters are propagations of uncertainties in both measured radiance (and DoLP) and the prior of the retrieved parameters.

Based on synthetic retrievals performed globally for 4 individual days, the standard deviation of the differences between the truth and the retrieved values were calculated for several AOD_{550} classes. The results for AOD_{550}, $AE_{550–865}$, and SSA_{550} are shown in Fig. C1. Note that relative differences were used for AOD_{550} and that absolute differences were used for $AE_{550–865}$ and SSA_{550}. For high AOD_{550} cases where few retrievals were available, the uncertainty was also calculated for $AOD_{550} > 1.6$ over land and $AOD_{550} > 0.8$ over ocean to ensure that more than 50 cases were used in each instance.

Retrievals over land have higher uncertainty than retrievals over ocean for almost all AOD_{550} bands in all variables. In addition, retrievals for $AOD_{550} > 1$ have lower uncertainty than $AOD_{550} < 1$. The standard deviation of these relative and absolute differences for each AOD_{550} band were used to define the uncertainty of the assimilated observations for both the SUPER and SPEXone satellites. For example, the uncertainty for the AOD_{550} band from 0.80 to 1.00 over land is 16.6 % for AOD_{550}, 0.362 for $AE_{550–865}$, and 0.021 for SSA_{550}.

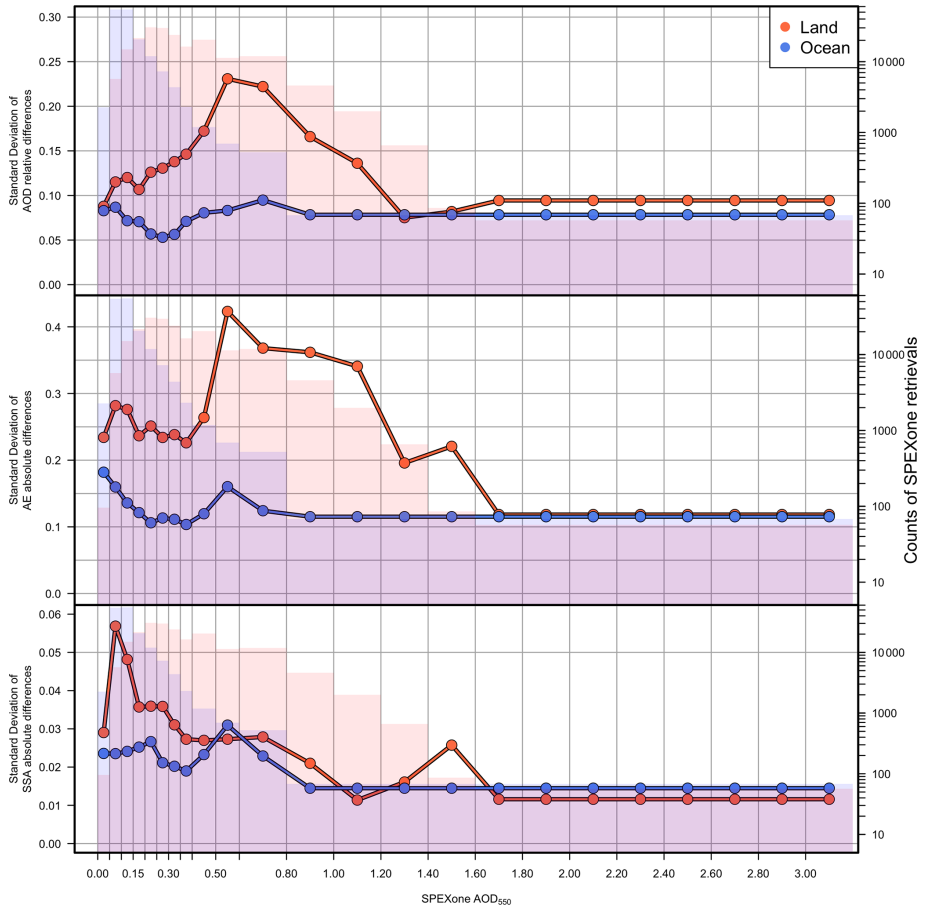

Figure C1. Defined uncertainty of SPEXone observations. Each point represents the standard deviation of the differences between truth and retrieved values for a specified AOD_{550} band. The analysis was carried out separately for retrievals over land and ocean. Bars depict the number of SPEXone retrievals for each AOD_{550} classes, and their height is associated with the right vertical axis.

Code and data availability. The model simulations and the SPEXone simulated retrievals are available from Zenodo at the following link: https://zenodo.org/record/5902137#.YfE4dPXMJ-U (last access: 20 April 2022; Tsikerdekis et al., 2022). The data assimilation software for aerosol emission estimation in ECHAM-HAM are available from Zenodo at the following link: https://doi.org/10.5281/zenodo.5596328 (Tsikerdekis et al., 2021b). The ECHAM-HAM version that was used in this study can be found in the following repository: https://svn.iac.ethz.ch/external/echam-hammoz/echam6-hammoz/branches/uni_amsterdam_vrije/ (last access: 8 April 2022). This repository can be accessed after registration at https://redmine.hammoz.ethz.ch/projects/hammoz (Hammoz, 2022). ERA-interim and ERA-5 data are freely available from https://doi.org/10.24381/cds.bd0915c6 (Hersbach et al., 2022) after registration.

Supplement. The supplement related to this article is available online at: https://doi.org/10.5194/gmd-15-3253-2022-supplement.

Author contributions. AT designed the experiments with the help of NAJS and OPH and carried them out. GF prepared SPEXone-simulated retrievals. AT performed the analysis and prepared the manuscript with contributions from all co-authors.

Competing interests. The contact author has declared that neither they nor their co-authors have any competing interests.

Disclaimer. Publisher's note: Copernicus Publications remains neutral with regard to jurisdictional claims in published maps and institutional affiliations.

Acknowledgements. This work was carried out on the Dutch national e-infrastructure with the support of SURF Cooperative.

Financial support. This research has been supported by the Dutch Research Council (NWO) and Netherlands Space Office (NSO) (grant no. 2017.008). Athanasios Tsikerdekis is funded by a NWO/NSO project "AEROSOURCE: Estimation of Aerosol Emissions from Polarization Data" (grant no. ALWGO.2017.008).

Review statement. This paper was edited by Samuel Remy and reviewed by two anonymous referees.

References

Arnold, C. P. and Dey, C. H.: Observing-Systems Simulation Experiments: Past, Present, and Future, B. Am. Meteorol. Soc., 67, 687–695, https://doi.org/10.1175/1520-0477(1986)067<0687:OSSEPP>2.0.CO;2, 1986.

Bruhwiler, L. M. P., Michalak, A. M., Peters, W., Baker, D. F., and Tans, P.: An improved Kalman Smoother for atmospheric inversions, Atmos. Chem. Phys., 5, 2691–2702, https://doi.org/10.5194/acp-5-2691-2005, 2005.

Chen, C., Dubovik, O., Henze, D. K., Lapyonak, T., Chin, M., Ducos, F., Litvinov, P., Huang, X., and Li, L.: Retrieval of desert dust and carbonaceous aerosol emissions over Africa from POLDER/PARASOL products generated by the GRASP algorithm, Atmos. Chem. Phys., 18, 12551–12580, https://doi.org/10.5194/acp-18-12551-2018, 2018.

Chen, C., Dubovik, O., Henze, D. K., Chin, M., Lapyonok, T., Schuster, G. L., Ducos, F., Fuertes, D., Litvinov, P., Li, L., Lopatin, A., Hu, Q., and Torres, B.: Constraining global aerosol emissions using POLDER/PARASOL satellite remote sensing observations, Atmos. Chem. Phys., 19, 14585–14606, https://doi.org/10.5194/acp-19-14585-2019, 2019.

Cheng, T., Peng, Y., Feichter, J., and Tegen, I.: An improvement on the dust emission scheme in the global aerosol-climate model ECHAM5-HAM, Atmos. Chem. Phys., 8, 1105–1117, https://doi.org/10.5194/acp-8-1105-2008, 2008.

Dubovik, O., Lapyonok, T., Kaufman, Y. J., Chin, M., Ginoux, P., Kahn, R. A., and Sinyuk, A.: Retrieving global aerosol sources from satellites using inverse modeling, Atmos. Chem. Phys., 8, 209–250, https://doi.org/10.5194/acp-8-209-2008, 2008.

Dubovik, O., Li, Z., Mishchenko, M. I., Tanré, D., Karol, Y., Bojkov, B., Cairns, B., Diner, D. J., Espinosa, W. R., Goloub, P., Gu, X., Hasekamp, O., Hong, J., Hou, W., Knobelspiesse, K. D., Landgraf, J., Li, L., Litvinov, P., Liu, Y., Lopatin, A., Marbach, T., Maring, H., Martins, V., Meijer, Y., Milinevsky, G., Mukai, S., Parol, F., Qiao, Y., Remer, L., Rietjens, J., Sano, I., Stammes, P., Stamnes, S., Sun, X., Tabary, P., Travis, L. D., Waquet, F., Xu, F., Yan, C., and Yin, D.: Polarimetric remote sensing of atmospheric aerosols: Instruments, methodologies, results, and perspectives, J. Quant. Spectrosc. Ra., 224, 474–511, https://doi.org/10.1016/j.jqsrt.2018.11.024, 2019.

Escribano, J., Boucher, O., Chevallier, F., and Huneeus, N.: Impact of the choice of the satellite aerosol optical depth product in a sub-regional dust emission inversion, Atmos. Chem. Phys., 17, 7111–7126, https://doi.org/10.5194/acp-17-7111-2017, 2017.

Feng, L., Palmer, P. I., Bösch, H., and Dance, S.: Estimating surface CO_2 fluxes from space-borne CO_2 dry air mole fraction observations using an ensemble Kalman Filter, Atmos. Chem. Phys., 9, 2619–2633, https://doi.org/10.5194/acp-9-2619-2009, 2009.

Guelle, W., Schulz, M., Balkanski, Y., and Dentener, F.: Influence of the source formulation on modeling the atmospheric global distribution of sea salt aerosol, J. Geophys. Res.-Atmos., 106, 27509–27524, https://doi.org/10.1029/2001JD900249, 2001.

Hammoz: Homepage, https://redmine.hammoz.ethz.ch/projects/hammoz, last access: 8 April 2022.

Hasekamp, O. P. and Landgraf, J.: Linearization of vector radiative transfer by means of the forward-adjoint perturbation theory and its use in atmospheric remote sensing, in: Light Scattering Reviews 2, pp. 159–204, Springer Berlin Heidelberg, Berlin, Heidelberg, https://doi.org/10.1007/978-3-540-68435-0_5, 2007.

Hasekamp, O. P., Fu, G., Rusli, S. P., Wu, L., Di Noia, A., Brugh, J. aan de, Landgraf, J., Martijn Smit, J., Rietjens, J., and van Amerongen, A.: Aerosol measurements by SPEXone on the NASA PACE mission: expected re-

trieval capabilities, J. Quant. Spectrosc. Ra., 227, 170–184, https://doi.org/10.1016/j.jqsrt.2019.02.006, 2019a.

Hasekamp, O. P., Gryspeerdt, E., and Quaas, J.: Analysis of polarimetric satellite measurements suggests stronger cooling due to aerosol-cloud interactions, Nat. Commun., 10, 5405, https://doi.org/10.1038/s41467-019-13372-2, 2019b.

Heinold, B., Tegen, I., Schepanski, K., and Banks, J. R.: New developments in the representation of Saharan dust sources in the aerosol–climate model ECHAM6-HAM2, Geosci. Model Dev., 9, 765–777, https://doi.org/10.5194/gmd-9-765-2016, 2016.

Hersbach, H., Bell, B., Berrisford, P., Hirahara, S., Horányi, A., Muñoz-Sabater, J., Nicolas, J., Peubey, C., Radu, R., Schepers, D., Simmons, A., Soci, C., Abdalla, S., Abellan, X., Balsamo, G., Bechtold, P., Biavati, G., Bidlot, J., Bonavita, M., Chiara, G., Dahlgren, P., Dee, D., Diamantakis, M., Dragani, R., Flemming, J., Forbes, R., Fuentes, M., Geer, A., Haimberger, L., Healy, S., Hogan, R. J., Hólm, E., Janisková, M., Keeley, S., Laloyaux, P., Lopez, P., Lupu, C., Radnoti, G., Rosnay, P., Rozum, I., Vamborg, F., Villaume, S., and Thépaut, J.: The ERA5 global reanalysis, Q. J. Roy. Meteor. Soc., 146, 1999–2049, https://doi.org/10.1002/qj.3803, 2020.

Hersbach, H., Bell, B., Berrisford, P., Biavati, G., Horányi, A., Muñoz Sabater, J., Nicolas, J., Peubey, C., Radu, R., Rozum, I., Schepers, D., Simmons, A., Soci, C., Dee, D., and Thépaut, J.-N.: ERA5 hourly data on pressure levels from 1979 to present, Copernicus Climate Change Service (C3S) Climate Data Store (CDS) [data set], https://doi.org/10.24381/cds.bd0915c6, 2018.

Hoesly, R. M., Smith, S. J., Feng, L., Klimont, Z., Janssens-Maenhout, G., Pitkanen, T., Seibert, J. J., Vu, L., Andres, R. J., Bolt, R. M., Bond, T. C., Dawidowski, L., Kholod, N., Kurokawa, J.-I., Li, M., Liu, L., Lu, Z., Moura, M. C. P., O'Rourke, P. R., and Zhang, Q.: Historical (1750–2014) anthropogenic emissions of reactive gases and aerosols from the Community Emissions Data System (CEDS), Geosci. Model Dev., 11, 369–408, https://doi.org/10.5194/gmd-11-369-2018, 2018.

Hoffmann, L., Günther, G., Li, D., Stein, O., Wu, X., Griessbach, S., Heng, Y., Konopka, P., Müller, R., Vogel, B., and Wright, J. S.: From ERA-Interim to ERA5: the considerable impact of ECMWF's next-generation reanalysis on Lagrangian transport simulations, Atmos. Chem. Phys., 19, 3097–3124, https://doi.org/10.5194/acp-19-3097-2019, 2019.

Huneeus, N., Chevallier, F., and Boucher, O.: Estimating aerosol emissions by assimilating observed aerosol optical depth in a global aerosol model, Atmos. Chem. Phys., 12, 4585–4606, https://doi.org/10.5194/acp-12-4585-2012, 2012.

Jin, J., Segers, A., Heemink, A., Yoshida, M., Han, W., and Lin, H. X.: Dust Emission Inversion Using Himawari-8 AODs Over East Asia: An Extreme Dust Event in May 2017, J. Adv. Model. Earth Syst., 11, 446–467, https://doi.org/10.1029/2018MS001491, 2019.

Kacenelenbogen, M. S., Vaughan, M. A., Redemann, J., Young, S. A., Liu, Z., Hu, Y., Omar, A. H., LeBlanc, S., Shinozuka, Y., Livingston, J., Zhang, Q., and Powell, K. A.: Estimations of global shortwave direct aerosol radiative effects above opaque water clouds using a combination of A-Train satellite sensors, Atmos. Chem. Phys., 19, 4933–4962, https://doi.org/10.5194/acp-19-4933-2019, 2019.

Kaiser, J. W., Heil, A., Andreae, M. O., Benedetti, A., Chubarova, N., Jones, L., Morcrette, J.-J., Razinger, M., Schultz, M. G., Suttie, M., and van der Werf, G. R.: Biomass burning emissions estimated with a global fire assimilation system based on observed fire radiative power, Biogeosciences, 9, 527–554, https://doi.org/10.5194/bg-9-527-2012, 2012.

Keene, W. C., Maring, H., Maben, J. R., Kieber, D. J., Pszenny, A. A. P., Dahl, E. E., Izaguirre, M. A., Davis, A. J., Long, M. S., Zhou, X., Smoydzin, L., and Sander, R.: Chemical and physical characteristics of nascent aerosols produced by bursting bubbles at a model air-sea interface, J. Geophys. Res., 112, D21202, https://doi.org/10.1029/2007JD008464, 2007.

Khade, V. M., Hansen, J. A., Reid, J. S., and Westphal, D. L.: Ensemble filter based estimation of spatially distributed parameters in a mesoscale dust model: experiments with simulated and real data, Atmos. Chem. Phys., 13, 3481–3500, https://doi.org/10.5194/acp-13-3481-2013, 2013.

Lamarque, J.-F., Bond, T. C., Eyring, V., Granier, C., Heil, A., Klimont, Z., Lee, D., Liousse, C., Mieville, A., Owen, B., Schultz, M. G., Shindell, D., Smith, S. J., Stehfest, E., Van Aardenne, J., Cooper, O. R., Kainuma, M., Mahowald, N., McConnell, J. R., Naik, V., Riahi, K., and van Vuuren, D. P.: Historical (1850–2000) gridded anthropogenic and biomass burning emissions of reactive gases and aerosols: methodology and application, Atmos. Chem. Phys., 10, 7017–7039, https://doi.org/10.5194/acp-10-7017-2010, 2010.

Long, M. S., Keene, W. C., Kieber, D. J., Erickson, D. J., and Maring, H.: A sea-state based source function for size- and composition-resolved marine aerosol production, Atmos. Chem. Phys., 11, 1203–1216, https://doi.org/10.5194/acp-11-1203-2011, 2011.

Meland, B. S., Xu, X., Henze, D. K., and Wang, J.: Assessing remote polarimetric measurement sensitivities to aerosol emissions using the geos-chem adjoint model, Atmos. Meas. Tech., 6, 3441–3457, https://doi.org/10.5194/amt-6-3441-2013, 2013.

Peng, Z., Liu, Z., Chen, D., and Ban, J.: Improving $PM_{2.5}$ forecast over China by the joint adjustment of initial conditions and source emissions with an ensemble Kalman filter, Atmos. Chem. Phys., 17, 4837–4855, https://doi.org/10.5194/acp-17-4837-2017, 2017.

Peters, W., Miller, J. B., Whitaker, J., Denning, A. S., Hirsch, A., Krol, M. C., Zupanski, D., Bruhwiler, L., and Tans, P. P.: An ensemble data assimilation system to estimate CO_2 surface fluxes from atmospheric trace gas observations, J. Geophys. Res., 110, D24304, https://doi.org/10.1029/2005JD006157, 2005.

Pope, R. J., Marsham, J. H., Knippertz, P., Brooks, M. E., and Roberts, A. J.: Identifying errors in dust models from data assimilation, Geophys. Res. Lett., 43, 9270–9279, https://doi.org/10.1002/2016GL070621, 2016.

Schepanski, K., Tegen, I., Laurent, B., Heinold, B., and Macke, A.: A new Saharan dust source activation frequency map derived from MSG-SEVIRI IR-channels, Geophys. Res. Lett., 34, L18803, https://doi.org/10.1029/2007GL030168, 2007.

Schultz, M. G., Stadtler, S., Schröder, S., Taraborrelli, D., Franco, B., Krefting, J., Henrot, A., Ferrachat, S., Lohmann, U., Neubauer, D., Siegenthaler-Le Drian, C., Wahl, S., Kokkola, H., Kühn, T., Rast, S., Schmidt, H., Stier, P., Kinnison, D., Tyndall, G. S., Orlando, J. J., and Wespes, C.: The chemistry–climate model ECHAM6.3-HAM2.3-MOZ1.0, Geosci. Model Dev., 11, 1695–1723, https://doi.org/10.5194/gmd-11-1695-2018, 2018.

Schutgens, N., Nakata, M., and Nakajima, T.: Estimating Aerosol Emissions by Assimilating Remote Sensing Observations into a Global Transport Model, Remote Sens., 4, 3528–3543, https://doi.org/10.3390/rs4113528, 2012.

Schutgens, N., Dubovik, O., Hasekamp, O., Torres, O., Jethva, H., Leonard, P. J. T., Litvinov, P., Redemann, J., Shinozuka, Y., de Leeuw, G., Kinne, S., Popp, T., Schulz, M., and Stier, P.: AEROCOM and AEROSAT AAOD and SSA study – Part 1: Evaluation and intercomparison of satellite measurements, Atmos. Chem. Phys., 21, 6895–6917, https://doi.org/10.5194/acp-21-6895-2021, 2021.

Schutgens, N. A. J. and Stier, P.: A pathway analysis of global aerosol processes, Atmos. Chem. Phys., 14, 11657–11686, https://doi.org/10.5194/acp-14-11657-2014, 2014.

Sekiyama, T. T., Tanaka, T. Y., Shimizu, A., and Miyoshi, T.: Data assimilation of CALIPSO aerosol observations, Atmos. Chem. Phys., 10, 39–49, https://doi.org/10.5194/acp-10-39-2010, 2010.

Sofiev, M., Soares, J., Prank, M., de Leeuw, G., and Kukkonen, J.: A regional-to-global model of emission and transport of sea salt particles in the atmosphere, J. Geophys. Res.-Atmos., 116, D21302, https://doi.org/10.1029/2010JD014713, 2011.

Stevens, B., Giorgetta, M., Esch, M., Mauritsen, T., Crueger, T., Rast, S., Salzmann, M., Schmidt, H., Bader, J., Block, K., Brokopf, R., Fast, I., Kinne, S., Kornblueh, L., Lohmann, U., Pincus, R., Reichler, T., and Roeckner, E.: Atmospheric component of the MPI-M earth system model: ECHAM6, J. Adv. Model. Earth Sy., 5, 146–172, https://doi.org/10.1002/jame.20015, 2013.

Stier, P., Feichter, J., Kinne, S., Kloster, S., Vignati, E., Wilson, J., Ganzeveld, L., Tegen, I., Werner, M., Balkanski, Y., Schulz, M., Boucher, O., Minikin, A., and Petzold, A.: The aerosol-climate model ECHAM5-HAM, Atmos. Chem. Phys., 5, 1125–1156, https://doi.org/10.5194/acp-5-1125-2005, 2005.

Tegen, I., Harrison, S. P., Kohfeld, K., Prentice, I. C., Coe, M., and Heimann, M.: Impact of vegetation and preferential source areas on global dust aerosol: Results from a model study, J. Geophys. Res.-Atmos., 107, AAC 14-1–AAC 14-27, https://doi.org/10.1029/2001JD000963, 2002.

Tegen, I., Neubauer, D., Ferrachat, S., Siegenthaler-Le Drian, C., Bey, I., Schutgens, N., Stier, P., Watson-Parris, D., Stanelle, T., Schmidt, H., Rast, S., Kokkola, H., Schultz, M., Schroeder, S., Daskalakis, N., Barthel, S., Heinold, B., and Lohmann, U.: The global aerosol–climate model ECHAM6.3–HAM2.3 – Part 1: Aerosol evaluation, Geosci. Model Dev., 12, 1643–1677, https://doi.org/10.5194/gmd-12-1643-2019, 2019.

Timmermans, R., Schaap, M., Segers, A., Elbern, H., Siddans, R., Tjemkes, S., Vautard, R., and Builtjes, P.: An Observing System Simulation Experiment (OSSE) for Aerosols, in: Air Pollution Modeling and Its Application XIX, pp. 287–295, Springer Netherlands, Dordrecht, https://doi.org/10.1007/978-1-4020-8453-9_31, 2008.

Timmermans, R. M. A., Lahoz, W. A., Attié, J.-L., Peuch, V.-H., Curier, R. L., Edwards, D. P., Eskes, H. J., and Builtjes, P. J. H.: Observing System Simulation Experiments for air quality, Atmos. Environ., 115, 199–213, https://doi.org/10.1016/j.atmosenv.2015.05.032, 2015.

Tsikerdekis, A., Schutgens, N. A. J., and Hasekamp, O. P.: Assimilating aerosol optical properties related to size and absorption from POLDER/PARASOL with an ensemble data assimilation system, Atmos. Chem. Phys., 21, 2637–2674, https://doi.org/10.5194/acp-21-2637-2021, 2021a.

Tsikerdekis, A., Schutgens, N. A.J., Fu, G., and Hasekamp, O. P.: Data Assimilation for aerosol emission estimation in ECHAM-HAM, Zenodo [code], https://doi.org/10.5281/zenodo.5596328, 2021b.

Tsikerdekis, A., Schutgens, N. A. J., Fu, G., and Hasekamp, O. P.: Data for the manuscript: Estimating aerosol emission from SPEXone on the NASA PACE mission using an ensemble Kalman Smoother: Observing System Simulation Experiments (OSSEs), Zenodo [data set], https://zenodo.org/record/5902137#.YfE4dPXMJ-U (last access: 20 April 2022), 2022.

van Amerongen, A., Rietjens, J., Campo, J., Dogan, E., Dingjan, J., Nalla, R., Caron, J., and Hasekamp, O.: SPEXone: a compact multi-angle polarimeter, in: International Conference on Space Optics – ICSO 2018, Chania, Greece, 9–12 October 2018, vol. 11180, edited by: Karafolas, N., Sodnik, Z., and Cugny, B., p. 20, https://doi.org/10.1117/12.2535940, SPIE, 2019.

Vignati, E., Wilson, J., and Stier, P.: M7: An efficient size-resolved aerosol microphysics module for large-scale aerosol transport models, J. Geophys. Res.-Atmos., 109, D22202, https://doi.org/10.1029/2003JD004485, 2004.

Werdell, P. J., Behrenfeld, M. J., Bontempi, P. S., Boss, E., Cairns, B., Davis, G. T., Franz, B. A., Gliese, U. B., Gorman, E. T., Hasekamp, O., Knobelspiesse, K. D., Mannino, A., Martins, J. V., McClain, C. R., Meister, G., and Remer, L. A.: The Plankton, Aerosol, Cloud, Ocean Ecosystem Mission: Status, Science, Advances, B. Am. Meteorol. Soc., 100, 1775–1794, https://doi.org/10.1175/BAMS-D-18-0056.1, 2019.

Xu, X., Wang, J., Henze, D. K., Qu, W., and Kopacz, M.: Constraints on aerosol sources using GEOS-Chem adjoint and MODIS radiances, and evaluation with multisensor (OMI, MISR) data, J. Geophys. Res.-Atmos., 118, 6396–6413, https://doi.org/10.1002/jgrd.50515, 2013.

Xu, X., Wang, J., Wang, Y., Henze, D. K., Zhang, L., Grell, G. A., McKeen, S. A., and Wielicki, B. A.: Sense size-dependent dust loading and emission from space using reflected solar and infrared spectral measurements: An observation system simulation experiment, J. Geophys. Res., 122, 8233–8254, https://doi.org/10.1002/2017JD026677, 2017.

Yumimoto, K. and Takemura, T.: The SPRINTARS version 3.80/4D-Var data assimilation system: development and inversion experiments based on the observing system simulation experiment framework, Geosci. Model Dev., 6, 2005–2022, https://doi.org/10.5194/gmd-6-2005-2013, 2013.

Zhang, K., O'Donnell, D., Kazil, J., Stier, P., Kinne, S., Lohmann, U., Ferrachat, S., Croft, B., Quaas, J., Wan, H., Rast, S., and Feichter, J.: The global aerosol-climate model ECHAM-HAM, version 2: sensitivity to improvements in process representations, Atmos. Chem. Phys., 12, 8911–8949, https://doi.org/10.5194/acp-12-8911-2012, 2012.